On Tear Film Breakup (TBU): Dynamics and Imaging

Richard J. Braun* and Tobin. A. Driscoll

Department of Mathematical Sciences, University of Delaware, Newark, DE 19711, USA
*Corresponding author: rjbraun@udel.edu

Carolyn G. Begley

School of Optometry, Indiana University, Bloomington, IN 47405, USA

P. Ewen King-Smith

College of Optometry, The Ohio State University, Columbus, OH 43218, USA

AND

J. I. Siddique

Department of Mathematics, Pennsylvania State University, York, PA 17403, USA

[Last modified: December 14, 2015]

We report the results of some recent experiments to visualize tear film dynamics. We then study a mathematical model for tear film thinning and tear film breakup (TBU), a term from the ocular surface literature. The thinning is driven by an imposed tear film thinning rate that is input from *in vivo* measurements. Solutes representing osmolarity and fluorescein are included in the model. Osmolarity causes osmosis from the model ocular surface, and the fluorescein is used to compute the intensity corresponding closely to *in vivo* observations. The imposed thinning can be either one-dimensional or axisymmetric, leading to streaks or spots of TBU, respectively. For a spatially-uniform (flat) film, osmosis would cease thinning and balance mass lost due to evaporation; for these space-dependent evaporation profiles TBU does occur because osmolarity diffuses out of the TBU into the surrounding tear film, in agreement with previous results. The intensity pattern predicted based on the fluorescein concentration is compared with the computed thickness profiles; this comparison is important for interpreting *in vivo* observations. The nondimensionalization introduced leads to insight about the relative importance of the competing processes; it leads to a classification of large vs small TBU regions in which different physical effects are dominant. Many regions of TBU may be considered small, revealing that the flow inside the film has an appreciable influence on fluorescence imaging of the tear film.

Keywords: tear film; thin film; tear osmolarity; fluorescence imaging; retroillumination; dry eye.

1. Introduction

The tear film is critical for nourishment and protection for the ocular surface (Bron et al., 2004; Govindarajan and Gipson, 2010) as well as proper optical function for the eye (Montés-Micó et al., 2010; Tutt et al., 2000). The tear film is a thin liquid film with multiple layers that establishes itself rapidly after a blink. At the anterior interface with air is an oily lipid layer that primarily retards evaporation (Braun et al., 2015), which helps to retain a smooth well-functioning tear film (Norn, 1979). Posterior to the lipid layer is the aqueous layer, which consists mostly of water (Holly, 1973). At the ocular surface, there is a region with transmembrane mucins protruding from the epithelial cells of the cornea or conjunctiva. This forest of glycosolated mucins, called the glycocalyx, has been referred to as the

mucus layer in past literature. It is generally agreed that the presence of the hydrophilic glycocalyx on the ocular surface prevents the tear film from dewetting (Tiffany, 1990*a*,*b*; Gipson, 2004). The overall thickness of the tear film is a few microns (King-Smith et al., 2004), while the average thickness of the lipid layer is on the order of tens to 100 nanometers (Norn, 1979; Yokoi et al., 1996; Goto and Tseng, 2003; King-Smith et al., 2011; Braun et al., 2015) and the thickness of the glycocalyx is a few tenths of a micron (Govindarajan and Gipson, 2010). This overall structure is reformed on the order of a second after each blink in a healthy tear film.

The aqueous part of tear fluid is primarily supplied from the lacrimal gland near the temporal canthus and the excess is drained through the puncta near the nasal canthus. Doane (1981) proposed the mechanism of tear drainage *in vivo* whereby tear fluid is drained into the canaliculi through the puncta during the opening interblink phase. Water lost from the tear film due to evaporation into air is an important process as well (Mishima and Maurice, 1961; Tomlinson et al., 2009; Kimball et al., 2010). We believe that this is the primary mechanism by which the osmolarity is increased in the tear film (Braun et al., 2015). Some water is supplied from the ocular epithelia via osmosis (Braun, 2012; Cerretani and Radke, 2014; Braun et al., 2015).

The role of osmolarity on the ocular surface may be summarized as in Baudouin et al. (2013) and Li et al. (2015). The healthy tear film maintains homeostasis with the blood in the range 296-302 Osm/m^3 (or, equivalently, mOsm/L or mOsM) (Lemp et al., 2011; Tomlinson et al., 2006; Versura et al., 2010), while healthy blood is in the range 285-295 Osm/m^3 (Tietz, 1995). In DES, the lacrimal system may be unable to maintain this homeostasis and osmolarity values in the meniscus rise to 316-360 Osm/m^3 (Tomlinson et al., 2006; Gilbard et al., 1978; Sullivan et al., 2010; Dartt and Willcox, 2013), and even higher values may be attained over the cornea. Using in vivo experiment and sensory feedback, Liu et al. (2009) estimated peak values of 800-900 Osm/m^3. Similar or higher values were computed from mathematical models of tear film break up in Braun et al. (2015) or Peng et al. (2014), or for models of the whole ocular surface (Li et al., 2015). The estimates from these models take on added significance since the osmolarity in TBU or in most locations since the only convenient method used in the clinic measures the osmolarity in the inferior meniscus (Lemp et al., 2011).

The ongoing supply and drainage of tear fluid affects the distribution and flow of the tear film. A number of methods have been used to visualize and/or measure tear film thickness and flow, including interferometry (Doane, 1989; King-Smith et al., 2004, 2009), optical coherence tomography (Wang et al., 2003), fluorescence imaging (Begley et al., 2013; King-Smith, Ramamoorthy, Braun and Nichols, 2013) and many others.

The use of fluorescein and other dyes have been used in a variety of ways, including: assessment of the condition of the ocular surface via staining of epithelial cells (Bron et al., 2015, e.g.,); estimation of tear drainage rates or turnover times (Webber and Jones, 1986); to visualize overall tear film dynamics (Benedetto et al., 1986; Begley et al., 2013; King-Smith, Ramamoorthy, Braun and Nichols, 2013; Li et al., 2014); estimation of first breakup times of the tear film (Norn, 1969); and the temporal progression of tear film breakup areas (Liu et al., 2006). There are different ways that fluorescence may be used to visualize the tear film. In the dilute limit, the fluorescein concentration is below the critical concentration, and the intensity of the fluorescence from the tear film is proportional to its thickness. In the concentrated (or self-quenching) limit, the intensity drops as the tear film thins in response to evaporation, and the thickness is roughly proportional to the square root of the intensity for a spatially uniform (flat) tear film (Nichols et al., 2012; Braun et al., 2014). Mathematical theories were able to capture a number of aspects of the overall tear film flow observed experimentally over the exposed ocular surface (Maki, Braun, Ucciferro, Henshaw and King-Smith, 2010; Li et al., 2014).

Simultaneous lipid interferometry and FL imaging has been used to study tear film dynamics as

well (King-Smith, Reuter, Braun, Nichols and Nichols, 2013; King-Smith, Ramamoorthy, Braun and Nichols, 2013). Lipid interferometry may be used to image the lipid layer thickness in grayscale in high resolution (0.2mm diameter field of view; King-Smith et al. (2011)) or in color in a slightly lower resolution (2mm diameter; Yokoi et al. (1996)). Low resolution imaging (6mm diameter or larger field of view) has been implemented in grey scale (King-Smith et al., 2009) or color (Goto and Tseng, 2003; Braun et al., 2015). Simultaneous methods have used lower resolution (King-Smith, Reuter, Braun, Nichols and Nichols, 2013). In the latter study, the imaging showed TBU by apparently different mechanisms. In their figure 6, there is a sequence of images that shows what appears to be very thin "holes" in the lipid layer that lead to what appears to be TBU in the corresponding times and locations in the FL images. The dynamics are consistent with evaporation through small holes, where the thickness is 20 nm or less (King-Smith et al., 2011; King-Smith, Reuter, Braun, Nichols and Nichols, 2013; Braun et al., 2015) and which have relatively low resistance to evaporation of water from the tear film. The localized increased thinning results in TBU over a period of up to 20 seconds. We develop the details of a mathematical model that describes the essence of this mode of TBU, and the FL method used to image it.

A variety of mathematical models have incorporated various important effects of tear film dynamics as recently reviewed by Braun (2012). The most common assumptions for these models are a Newtonian tear fluid and a flat cornea (Berger and Corrsin, 1974; Braun et al., 2012). Tear film models are often formulated on a one-dimensional (1D) domain oriented vertically through the center of the cornea with stationary ends corresponding to the eyelid margins. We refer to models on this kind of domain as 1D models. Surface tension, viscosity, gravity and evaporation are often incorporated into 1D models; wetting forces have been included as well. Due to space considerations we refer the reader to a recent review (Braun, 2012).

Of interest in this paper is the osmolarity of the tear film. Zubkov et al. (2012) formulated and studied a mathematical model that describes the spatial distribution of tear film osmolarity that incorporates both fluid and solute (osmolarity) dynamics, evaporation, blinking and vertical saccadic eyelid motion. They found that both osmolarity was increased somewhat in the "black line" region of thinning near the meniscus (Miller et al., 2002) and that measurements of the solute concentrations within the inferior meniscus need not reflect those elsewhere in the tear film. This model gave smaller increases in osmolarity than spatially-uniform models discussed below (Braun, 2012; Braun et al., 2015) because of the higher evaporation rates and lack of diffusion along the tear film in the latter models. Larger increases in osmolarity were reported in the eye-shaped domain model studied by Li et al. (2015) because they used larger evaporation rates as may be seen experimentally (King-Smith et al., 2010).

There have also been models with one independent space dimension that studied TBU. Sharma and Ruckenstein extended tear film models with van der Waals driven rupture to linear (Sharma and Ruckenstein, 1986b) and nonlinear (Sharma and Ruckenstein, 1985, 1986a) theories with a distinct mucus layer between the aqueous layer and the flat underlying substrate (epithelium). An insoluble surfactant on the hypothesized mucus-aqueous interface was also included. The models were derived with shear forces dominating in both layers. The mucus layer was unstable to van der Waals forces in the model, and this was interpreted as TBU. All of the theories could give reasonable TBUT ranges.

The two-layer film theory was modified to include van der Waals forces in both mucus and aqueous layers, and surfactant transport by Zhang et al. (2003, 2004). The mucus layer was treated as a power-law fluid with a fit to experimental data for whole tears (Pandit et al., 1999) over a range of shear rates up to 5s^{-1} being used to determine the power $n = 0.81$. The aqueous layer was assumed to be Newtonian, and the lipid layer was simplified to the transport of an insoluble surfactant at the aqueous/air interface. They found that the tear film could be unstable with rupture driven by van der Waals forces. Thinner

mucus layers in the model led to reduced TBUTs, and increased Marangoni effect (stronger surfactant) led to increased TBUTs. Related papers, which may apply to eyes via analogy with lung surfactants, include Matar et al. (2002). For a comprehensive review of related bilayer work, see Craster and Matar (2009).

More recently, the DEWS report (Lemp et al., 2007) has argued that TBU is driven, at least in many cases, by evaporation, which causes increased osmolarity (concentration of ions) in the tear film, which may lead to irritation, inflammation and damage to the ocular epithelium. Currently, the authors are unaware of any method to directly measure the osmolarity in regions of TBU due to the very small volumes of tear fluid involved, the rapid dynamics there, and the extreme sensitivity of the cornea. Theoretical efforts have responded to this situation by creating models that incorporate evaporation and osmosis, as well as other effects, into the mathematical models to better understand the dynamics of the process at a small scale.

In Braun (2012) and Braun et al. (2015), a model for an evaporating, spatially uniform film was studied. The model was a single ordinary differential equation for the tear film thickness that included evaporation from the tear/air interface at a constant rate and osmotic flow from the tear/cornea interface that was proportional to the osmolarity increase above the isotonic value. The latter assumption simplifies the tear/cornea interface to a semi-permeable boundary that allows water but not solutes to pass. They found that the model predicted equilibration of the tear film thickness at values greater than the height of the glycocalyx for sufficiently large permeability of the tear/cornea interface. They also found that the osmolarity could become quite large as the tear film thinned for small permeability values, as much as 10 times the isotonic value under some conditions. The model given in Braun (2012) included van der Waals forces that stopped thinning at the purported height of the glycocalix which allowed the model to be used at zero permeability at the tear/cornea interface. Similar conclusions about the osmolarity during thinning were found there.

These models were extended to include a specified evaporation profile that varied in space by Peng et al. (2014) and Braun et al. (2015). A space-dependent evaporation distribution was created by Peng et al. (2014) that had two parts. One part used an immobile lipid layer with specified thickness and fixed resistance to diffusion through it by water. The other part was a resistance to transport in the air outside the tear film; this second resistance included convective and diffusive transport in the air. They found that the osmolarity was elevated in this model for TBU. For the single-layer models studied in Braun et al. (2015), The evaporation profile was either Gaussian or a hyperbolic tangent, with either having a peak (central) value that could be specified larger than the surrounding constant rate. The local thinning caused by locally increased evaporation led to increased osmolarity in the break up region, which could also be several times larger than the isotonic value. Braun et al. (2015) also included fluorescein transport in that model, and could compute intensity distributions as well as fluorescein concentration. They gave preliminary results that showed that FL imaging techniques for TBU may need to be interpreted with care because the flow inside the tear film could transport fluorescein there and thus change the appearance of TBU given by FL imaging.

In this paper, we investigate more thoroughly the complex model for tear film flow, evaporation, osmolarity and fluorescein transport, osmosis and fluorescence in TBU. We expand greatly on those previous preliminary results in Braun et al. (2015) and as well introduce a new scaling into the problem that substantially aids understanding the computed and empirical data. The emphasis in this paper is on understanding the flow and transport of solutes inside the film, and at the same time closely compare those results with available experimental results. The models are able to go well beyond the experimental data available and make predictions. The model adds significant new results about the distribution of osmolarity in TBU, which at this time cannot be measured directly to our knowledge. We

believe that these results will impact the understanding of osmolarity dynamics in the tear film as well as the understanding of FL imaging of TBU dynamics.

The paper is organized as follows. We describe some experimental TBU observations using simultaneous imaging methods. We then develop the mathematical model formulations for spots and streaks, present results; discussion and conclusion sections follow. The details of the mathematical formulation appear in the appendices.

2. Experimental observations of TBU

The fluorescein method for tear film imaging involves instillation of a sodium flourescein solution of known concentration or insertion of a fluorescein-soaked strip into the lower fornix (Carlson and Kurtz, 2004). We instilled a 2 microliter drop of 2% FL solution; the illumination used a cobalt blue filter (494 nm wavelength) with a Wratten number 8 filter (yellow) over the observation port. Exposing the tear film to this blue light then causes the aqueous portion of the tear film to emit green light (Lakowicz, 2006, 521 nm wavelength). Because the resulting concentration of fluorescein in the tear film is usually unknown (Wu et al., 2015), and the intensity of light emitted by the fluorescein molecules depends on the concentration (Webber and Jones, 1986; Nichols et al., 2012) and the thickness (Braun et al., 2014), the interpretation of thinning experiments may be complicated. In spite of these difficulties, fluorescent intensity (FL) imaging of the tear film is considered the classic clinical method (Norn, 1969; Webber and Jones, 1986) but more recent methods use concentration quenching of fluorescein molecules to estimate relative local and overall tear film thinning (Nichols et al., 2012). We also used simultaneous retroillumination (RI) imaging of the tear film through the pupil during TBU (Himebaugh et al., 2003); the RI method was implemented on a separate system but the two systems were aligned and registered. The results from each method then aid interpretation of the dynamics of tear film instability.

In the experiments, subjects were asked to keep their eyes open as long as they could and the simultaneous observations made throughout the experiment. The images were processed using custom Matlab software (The Mathworks, Inc., Natick, MA, USA). The principles of the Declaration of Helsinki were followed for this study and the study was approved by the Biomedical Institutional Review Board of Indiana University. Informed consent was obtained from all subjects after explanation of the procedures involved in the study.

The FL intensity I is given by the following equation (Webber and Jones, 1986; Nichols et al., 2012):

$$I = I_0 \frac{1 - e^{-\varepsilon_f h' f'}}{1 + (f'/f_{cr})^2}. \tag{2.1}$$

Here h' is the tear film thickness, f' is the fluorescein concentration, ε_f is the Naperian extinction coefficient and I_0 is a normalization factor that takes into account a number of factors including the optical system. For fixed h', expanding for small f' yields a leading term proportional to f' and h'; this is the dilute regime. Expanding for large f' shows that the intensity decreases proportional to $1/(f')^2$; this is the self-quenching regime (Nichols et al., 2012). When the spatially-uniform tear film thins by evaporation, mass conservation requires that $h'f' = f_0'h_0'$ where the subscript zeros indicate initial values. Thus, for the spatially uniform case in the self-quenching regime, the thickness is proportional to the square root of the intensity (Nichols et al., 2012; Braun et al., 2014). This approximation was used to estimate the tear film thickness from the FL images in previous work (Nichols et al., 2012; Braun et al., 2015).

The top row of Fig. 1 shows a subset of FL images from a video recording of TBU (dark areas) progressing over approximately 24 s. The thickness is estimated from these images by computing $\sqrt{I}$
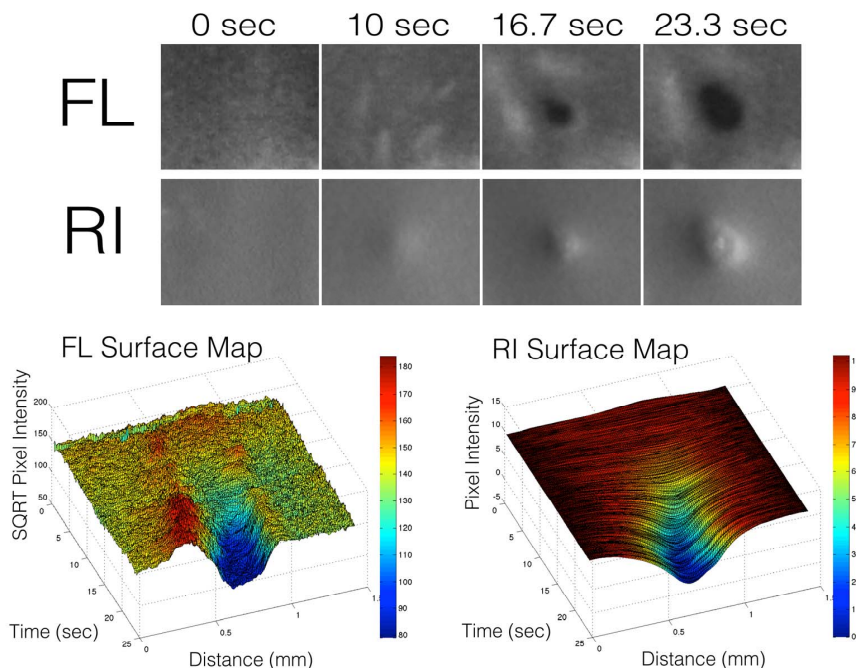
FIG. 1: Experimental images using FL imaging (top row) and RI imaging (second row) of the same area, shown at four different times. The diameter of each of the images is the line monitored over time in the plots in the bottom two images. The false color contour plots show the thickness changes with time along a diameter of the TBU region as estimated from each method.

and normalizing it to the assumed initial value; here we do not normalize to an initial thickness, but only show relative changes. RI images (second row) at the same times and over the same areas are shown as well. A flat surface (constant tear thickness) is represented by a certain intensity in the RI image whereas positive or negative surface slopes are represented by higher or lower intensities, respectively. From the RI image, the thickness is estimated from integrating the intensity using the trapezoidal rule, and choosing the constant of integration so that the assumed initial condition is obtained. The arbitrary constant cannot be determined from these methods, and only relative changes are studied here. Quantitative results for the tear film thinning were calculated along the same diameter in each image (not all images shown).

In order to measure the correlation between the two types of images and to estimate tear film thinning rates, the thickness across a diameter was calculated at each time, and the results shown as a color contour plot (Fig 1c and 1d). The results show a local thinning area in both the FL and RI images. The correlation between fluorescein and retroillumination images at the end of TBU was very high ($r = 0.889$ in this case). The contour plots also show that the thinning in the TBU region begins later for the FL imaging compared to the RI imaging. This apparent delay is investigated in more detail in the next figure.

Figure 2 shows the thickness distribution at different times along the line segments shown in the insets for FL imaging (A) and RI imaging (C). At later times, the thickness is clearly decreasing in the
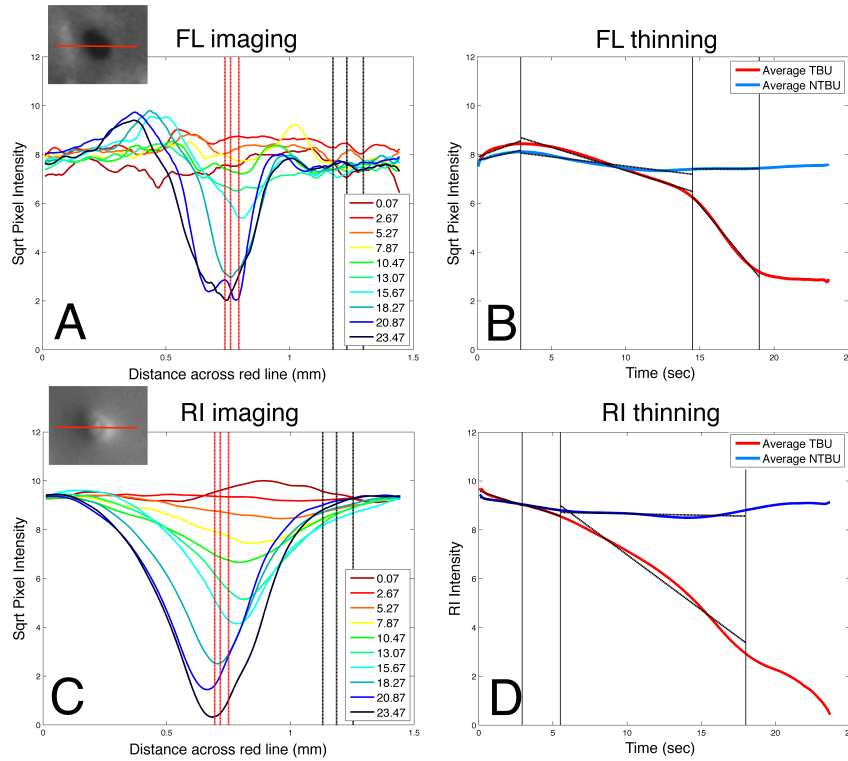

FIG. 2: The left column shows estimates of thickness at different times from FL imaging (A) and RI imaging (C) for the line segment shown in the respective inset. The right column shows thickness as a function of time averaged from the three positions indicated by the red lines in the TBU region and from the three blue lines in non-TBU region: (B) FL imaging, (D) RI imaging.

TBU region for both methods, as would be expected from the contour plots and high correlation values. The results also show in a different way that the RI imaging produces smoother thickness plots that begin to decrease in thickness earlier and vary more smoothly across the TBU region. Figure 2 also shows averaged thickness as a function of time from locations inside and outside the TBU region. For each imaging method, the same three locations are used, and they are indicated with red lines inside the TBU region and blue lines outside the TBU region. The estimated thinning rates outside TBU are approximately zero in either imaging method, indicating roughly constant thickness. The thinning rate from RI imaging (Figure 2D) more closely approximates a constant rate, though it is not perfectly linear. There appears to be two different thinning rates from FL imaging (Figure 2B); a slower initial rate is followed by a faster one. This can appear to be a delay in the onset of TBU relative to RI imaging.

Similar trends are seen in other cases not shown here. We believe that the solute dynamics of fluorescein can help explain the different apparent thinning rates (Braun et al., 2015); further details will be given later in this paper.

Fig. 3 shows the time dependence of the width of TBU as measured by the distance across TBU at 60% of the depth. The RI result is clearly wider than that given from the FL result. In Braun
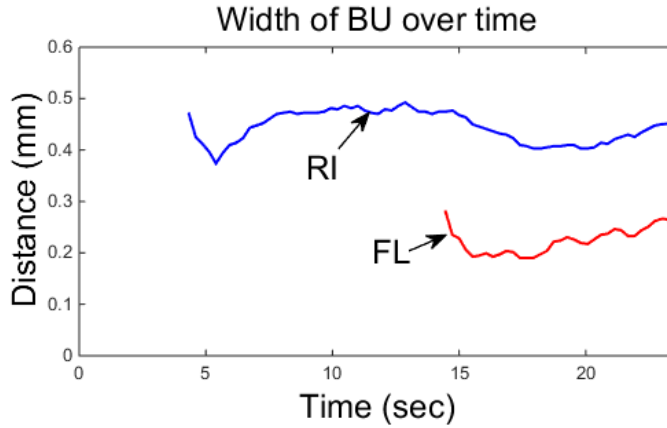

FIG. 3: The width of the TBU region studied in the previous figures is plotted with time for the two imaging methods using the width at 60% of the depth of TBU.

et al. (2015), we hypothesized that the apparently-narrower TBU region from FL imaging was due to advection of fluorescein into the TBU region via capillary driven flow. The results in that case were for streak TBU; here we study spot TBU, and the observations are similar.

It appears that the TBU region in the FL image in Fig. 1 has steeper sides than the corresponding RI image there. The onset of thinning is apparently delayed in the FL imaging compared to the RI imaging, as shown in Fig. 2. In Fig. 3, the TBU region is apparently narrow when inferred from FL imaging. We aim to explain why these and other phenomena occurs in this paper using a mathematical model problem.

3. Model formulation

We give the scalings and nondimensional parameters first, and then specify the axisymmetric problem for spot TBU case. The derivation is given in the appendices. The problem for the streak TBU is a Cartesian version of the spot TBU in one dimension; the problem for streaks is specified in the appendices.

3.1 *Scalings*

The tear film is assumed to have constant density ρ and dynamic viscosity μ, and the tear/air interface is assumed to have constant surface tension σ_0. We use the following scalings to nondimensionalize

system of equations (primes denote dimensional variables):

$$r' = \ell r, \quad z' = dz, \quad \varepsilon = d/\ell, \quad t' = \frac{d}{v_0}t, \quad h' = dh, \quad u' = (v_0/\varepsilon)u, \quad v' = v_0 v, \tag{3.1}$$

$$p' - p'_v = \frac{\mu v_0}{\ell \varepsilon^3}p, \quad J' = \rho v_0 J, \quad c' = c_0 c, \quad f' = f_{cr}f. \tag{3.2}$$

Here (r,z) are the radial and axial coordinates, along and through the film, respectively; (u,w) are the respective velocity components and t is time. $h(r,t)$ is the tear film thickness; p is the pressure; p'_v is reference vapor pressure in the environment; J is the evaporative flux, c is the osmolarity; and f is the fluorescein concentration. The typical tear film thickness is d, ℓ is the length scale along the film, v_0 is the peak thinning rate taken as input from experiment, c_0 is the isotonic osmolarity, and f_{cr} is the critical fluorescein concentration. We compute the size of ℓ by balancing surface tension and viscous forces inside the film as discussed below. Here $\varepsilon \ll 1$ represents a ratio of typical distance through the film to that along the film which is typically small for the tear film. We chose the scales for time and velocity based on the maximum thinning rate v_0 and the tear film thickness d.

The nondimensional parameters that arise are as follows:

$$S = \frac{\sigma_0 \varepsilon^4}{\mu v_0}, \quad A = \frac{A^*}{\mu v_0 \ell^2}, \quad P_c = \frac{P_o V_w c_0}{v_0}, \quad \mathrm{Pe}_f = \frac{v_0 \ell}{\varepsilon D_f}, \quad \mathrm{Pe}_c = \frac{v_0 \ell}{\varepsilon D_o}, \quad \phi = \varepsilon_f f_{cr} d'. \tag{3.3}$$

Here A^* is the Hamaker constant, P_o is the permeability of water at the tear/cornea interface, V_w is the molar volume of water, D_o is the diffusivity of osmolarity (salt) in water, D_f is the diffusivity of fluorescein in water, ε_f is the Naperian extinction coefficient of fluorescein. Values for the dimensional constants and the nondimensional parameters are given in Tables 2 and 3 below. We first discuss our choice of ℓ.

We chose ℓ by enforcing $S = 1$, which causes the surface tension and viscous forces inside the film to be the same size at this length. Solving for ℓ gives

$$\ell = \left(\frac{\sigma_0}{\mu v_0}\right)^{1/4} d. \tag{3.4}$$

The thinning rate appears because the thinning is the cause of the viscous effects from flow along the film. One could interpret the thinning as balancing surface tension in a sense, but the 1/4 power suggests that the induced viscous stress along the film balances capillary pressure from deformation of the film. Using $d = 3.5\mu$m, $\mu = 1.3 \times 10^{-3}$Pa·s, and $v_0 = 10\mu$m/min, we find $\ell \approx 0.42$mm. If we reduce the thinning rate by a factor of ten to $v_0 = 1\mu$m/min, then $l = 0.74$mm; other values are given in Table 1.

v_0 (μm/min)	1	4	10	20	38
ℓ (mm)	0.747	0.528	0.420	0.353	0.301

Table 1: The horizontal length scale ℓ as a function of the maximum thinning rate v_0 for thickness $d = 3.5\mu$m.

The dimensional parameters are given in Table 2. The solutal properties for the osmolarity are assumed to be those of salt (NaCl) in water (Riquelme et al., 2007), which seems reasonable because the osmolarity is primarily composed of small ions of salts. The fluorescein properties are somewhat

Dimensional Parameters

Parameter	Description	Value	Reference
μ	Viscosity	1.3×10^{-3}Pa·s	Tiffany (1991)
σ_0	Surface tension	0.045N·m^{-1}	Nagyová and Tiffany (1999)
ρ	Density	10^3kg·m^{-3}	Water
A^*	Hamaker constant	$6\pi \times 3.5 \times 10^{-19}$Pa·m^3	Winter et al. (2010)
d'	Characteristic thickness	3.5×10^{-6}m	King-Smith et al. (2004)
ℓ	$(\sigma_0/\mu/v_0)^{1/4}d$	0.35×10^{-3} m	Calculated
v_0	Peak thinning rate	$4 - 38\mu$m/min	Nichols et al. (2005)
V_w	Molar volume of water	1.8×10^{-5}m^3·mol^{-1}	Water
h_{eq}	Equilibrium thickness	0.25×10^{-6}m	Estimated, Gipson (2004)
D_f	Diffusivity of fluorescein	0.39×10^{-9}m^2/s	Casalini et al. (2011)
D_o	Diffusivity of salt	1.6×10^{-9}m^2/s	Riquelme et al. (2007)
P_o	Permeability of cornea	12.1×10^{-6}m/s	Braun et al. (2015)
ε_f	Naperian extinction coefficient	1.75×10^7m^{-1}M^{-1}	Mota et al. (1991)

Table 2: The dimensional parameters used in this paper are shown here. Additional sources for the thinning rates include King-Smith et al. (2009) and Peng et al. (2014). The molar extinction coefficient given in Mota et al. (1991) has been multiplied by ln(10) to convert it to the Naperian form; this corrects our previous use of the extinction coefficient (Nichols et al., 2012; Braun et al., 2014, 2015).

different due to the larger size of the fluorescein ion (Casalini et al., 2011). A^* is calculated so that assumed minimum equilibrium thickness of the tear film h_{eq} will be 0.25μm (Winter et al., 2010). For the calculations in this paper, we vary the peak thinning rate from 4 to 38μm/min in accord with experiment (King-Smith et al., 2009) and previous work (Peng et al., 2014; Braun et al., 2015).

3.2 *Lubrication theory*

The thin film approximation, or lubrication theory results in a simplified system of equations to solve for the tear film dynamics. The derivation can be found in Appendix B. On $0 < r < R_O$, we must solve

$$\partial_t h + J - P_c(c-1) + \frac{1}{r}\partial_r (rh\bar{u}) = 0, \tag{3.5}$$

$$\bar{u} = -\frac{h^2}{12}r\partial_r p, \tag{3.6}$$

$$p = -\frac{1}{r}\partial_r (r\partial_r h) - Ah^{-3}, \tag{3.7}$$

$$h(\partial_t c + \bar{u}\partial_r c) = \text{Pe}_c^{-1}\frac{1}{r}\partial_r (rh\partial_r c) + Jc - P_c(c-1)c, \tag{3.8}$$

$$h(\partial_t f + \bar{u}\partial_r f) = \text{Pe}_f^{-1}\frac{1}{r}\partial_r (rh\partial_r f) + Jf - P_c(c-1)f. \tag{3.9}$$

The pressure will be treated as a dependent variable in the numerical treatment described below.

The dynamics are driven by the evaporative flux J, which is scaled with ρv_0, the maximum mass

Nondimensional parameters with typical values

Parameter	Expression	Value
ε	$\dfrac{d'}{L'}$	1×10^{-2}
S	$\dfrac{\sigma_0 \varepsilon^4}{\mu v_0}$	1
A	$\dfrac{A^*}{\mu v_0 \ell^2}$	0.9×10^{-3}
α	$\dfrac{\alpha_0 \mu}{\rho \ell \varepsilon^3}$	0.0368
α_0	$\dfrac{(h_{eq})^3 \rho v_0}{A^*}$	9.74×10^{-6}
P_c	$\dfrac{P_o V_m c_0}{v_0}$	0.1960
Pe_f	$\dfrac{v_0 \ell}{\varepsilon D_f}$	30.5
Pe_c	$\dfrac{v_0 \ell}{\varepsilon D_o}$	7.43
ϕ	$\varepsilon_f f_{cr} d'$	0.326

Table 3: Dimensionless parameters that arise from scaling the dimensional fluid mechanics problem. The values given are based upon the values of Table 2, $d = 3.5 \mu$m and $v_0 = 20 \mu$m/min.

flux measured from experiment. Nondimensionally,

$$J = J_f(r) - \alpha \left[\frac{1}{r} \partial_r (r \partial_r h) + \frac{A}{h^3} \right] \tag{3.10}$$

We use two choices for $J_f(r)$, Gaussian or an approximation to a constant evaporation rate inside a disk via a hyperbolic tangent profile (referred to as tanh). For the Gaussian case,

$$J_f(r) = v_b + (1 - v_b) e^{-(r/r_w)^2/2} \tag{3.11}$$

The standard deviation r_w will be used to indicate the radius of the evaporation distribution. The background thinning rate $v_b = v_1/v_0$ is the relative to the peak rate; the dimensional value is assumed to be 1μm/min in all cases. For the tanh case,

$$J_f(r) = v_b + (1 - v_b) \left[1 - \tanh \left(\frac{r - r_w}{2r_0} \right) \right] \tag{3.12}$$

We use $r_0 = 0.05$ to keep the transition narrow. The mass lost can be kept the same if r_w for the tanh case is $\sqrt{2}$ larger than the Gaussian case. When making a direct comparison between the two cases, we maintained this relationship.

The FL intensity I is computed from the thickness h and the fluorescein concentration f via the nondimensional version of Eqn. (2.1) (Webber and Jones, 1986; Nichols et al., 2012)

$$I = I_0 \frac{1 - e^{-\phi f h}}{1 + f^2}. \tag{3.13}$$

Here ϕ is the nondimensional Naperian extinction coefficient. As mentioned previously, for fixed thickness h the FL intensity decreases linearly at small concentration in the so-called dilute regime. Sufficiently above a critical concentration $f_{cr} = 0.2\%$, the intensity decreases quadratically with increasing f, the so-called quenching or self-quenching regime (Nichols et al., 2012). We use the latter term here. For a tear film thinning by evaporation, the situation is slightly more complicated. For a flat tear film, the product hf is constant, and so in the dilute regime, I is constant during thinning, while in the self-quenching regime, the quadratic decrease for increasing f still holds (Braun et al., 2014).

3.3 *Boundary and initial conditions*

The no-flux boundary conditions are homogeneous Neumann for all variables at the outer boundary $r = R_O$:

$$\partial_r h(R_O,t) = \partial_r p(R_O,t) = \partial_r c(R_O,t) = \partial_r f(R_O,t) = 0. \tag{3.14}$$

$R_O = 5$ is used for all results here unless otherwise noted.

The following BCs will prevent any singularities at the origin:

$$\lim_{r \to 0}(1/r)\partial_r h(0,t) = \lim_{r \to 0}(1/r)\partial_r p(0,t) = \lim_{r \to 0}(1/r)\partial_r c(0,t) = \lim_{r \to 0}(1/r)\partial_r f(0,t) = 0. \tag{3.15}$$

The initial conditions are all uniform in space:

$$h(r,0) = c(r,0) = 1, \; f(r,0) = f_0. \tag{3.16}$$

Here f_0 is the concentration of FL normalized to the critical fluorescein concentration $f_{cr} = 0.2\%$. The definition of the pressure, Eqn. (3.7), wass used to compute the corresponding initial pressure.

3.4 *Numerical method*

The pressure inside the film, via Eqn. (3.7), was treated as a dependent variable as in some previous papers (Miller et al., 2002; Maki, Braun, Henshaw and King-Smith, 2010; Li and Braun, 2012). The other equations for the dependent variables in Eqns. (3.5)–(3.9) was solved with an application of the method of lines. The space derivatives were discretized using Chebyshev points, and differentiation matrices used to compute the derivatives in real space (Trefethen, 2000).

For the axisymmetric case, the no flux conditions at the origin were implemented by applying $\lim_{r \to 0}(\partial_r g)/r = 0$, where g represents any dependent variable. Expanding the second order operators in r, applying this condition results in only even derivatives at the origin in the PDEs for the dependent variables, and no division by r there (Smith, 1996). We solved the discretized version of these modified PDEs at the origin for the dependent variables.

For the Cartesian case representing streak TBU, symmetry requirement could be applied directly at that grid point with no difficulty.

The resulting system is a differential algebraic system with time derivatives for h, c and f, and not for p. The system was solved using `ode15s` in MatLab (The MathWorks Inc., Natick, MA).

4. Results

In what follows, we will compare the results from numerically solving the PDEs with results for the flat, spatially-uniform film. This flat film case was studied in several previous papers (Braun, 2012; Braun et al., 2014, 2015). In that case, all spatial derivatives are zero, and the resulting system can be reduced to a single ordinary differential equation for h, along with the mass conservation conditions $hc = 1$ and $hf = f_0$ with initial conditions as in Eqn 3.16 (Braun et al., 2014). The computed results are an upper bound or worst case scenario for the osmolarity in TBU, but we will see that they provide no such bound for the fluorescein concentration.

4.1 *Spots*

We begin with results for axisymmetric spot TBU. These computed results will be for Gaussian thinning rates of various sizes, Eqn. (3.11), followed by hyperbolic tangent profiles, Eqn. (3.12).

4.1.1 *Large Gaussian and Tanh Spots*   In this section, we present the summary of computed results for the h, c, f and J. The set of parameters used in this section, unless otherwise noted, are $d = 3.5\mu$m and $v_0 = 20\mu$m/min, so that the time scale is $d/v_0 = 10.5s$. Under these conditions, $\ell \approx 0.35$mm. Unless otherwise noted, $v_1 = 1\mu$m/min, so that typically $v_b = 0.05$.

Figure 4 shows tear film thickness h, evaporative flux J, osmolarity c and FL concentration f as a function of space for different times. We see that the tear film thickness decreases to a low level that we interpret as TBU and that this takes slightly longer than one unit of time; this confirms the suitability of our choice of time scale for a thinning rate distribution of this width. When the thickness of the tear film gets small enough, the evaporative flux is reduced according to the model. The osmolarity and FL concentrations develop elevated values in the TBU region as has been found elsewhere, with the peak in f several times larger than the peak in c due to its smaller diffusivity. However, these peak values of osmolarity are not sufficient to stop the thinning of the tear film, and thinning progresses to TBU. The evaporative flux J decreases at the thinnest h values due to the presence of the wetting term Ah^{-3} in the pressure. This reduction of J prevents the tear film thickness from decreasing to zero and is designed to stop the thinning at about 0.25 μm to mimic the thickness of the glycocalyx (Winter et al., 2010). This allows the computations to proceed beyond the initial appearance of TBU, or TBU time (TBUT). While the TBUT is often used as a measure of tear film instability, the progression of TBU as measured by increasing area during the interblink interval is an important clinical aspect (Liu et al., 2006). We do not treat the spreading of TBU in this model because it is limited by the assumed evaporation distribution. We also note that TBUT as measured by clinicians typically cannot reach the same precision as the mathematical model because their observations are based on the initial appearance dark spots that may not correspond to reaching the same small values of thickness (Braun et al., 2015). This may result in significantly smaller estimates and significant variation in TBUT than we compute here (Guillon, 2002). Finally, when different evaporation models are used, the thinning may stop at much smaller values than we use here (Peng et al., 2014, and discussed further in Section 4.1.5).

Figure 5 shows the numerical solutions for the tanh distribution for $r_w = 1.41$ at the same parameter values as Fig. 4. This value of r_w yields the same total rate of water loss due to evaporation as that of the Gaussian thinning rate profile as shown in Fig. 4. The overall dynamics of the hyperbolic tangent

profile match with that of the Gaussian profile except for two features. First, the film initially thins in a roughly flat distribution inside the TBU region (near $r = 0$), but for $t = 2.9$, it develops a negative curvature. This causes a high pressure that causes flow toward the edge of the TBU region. This type of deformation has been observed in several situations of film drainage (Braun, 2012, e.g.). This outward flow meets an inward flow due to high pressure outside the TBU region, and this causes a local maximum in the fluorescein concentration near the edge of TBU. The evaporative flux is complicated in this case. The osmolarity and FL concentrations develop elevated values in the TBU region, and again these peak values are insufficient to stop thinning of the tear film, leading to TBU. For narrower thinning rate distributions, the results are similar to those of the Gaussian distribution, though it appears to be slightly faster to reach TBU than for the Gaussian case.

When r_w is decreased, similar dynamics occur. The tear film thins locally, the solute concentrations rise in the TBU region, but there are some differences in the details. There is stronger flow toward TBU from capillary forces for smaller r_w, and this slows down the decrease in thickness at $r = 0$. The maxima of c and f are increased for the increased flow with smaller r_w as well. Additional results presented below will quantify and clarify the differences.

4.1.2   *Diffusive vs advective transport*   In this subsection, we illustrate the relative importance of the diffusive and advective aspects of solute transport. Explaining the results for different spot sizes and other parameter changes relies on understanding this. The diffusive term for the osmolarity is

$$-\frac{1}{\text{Pe}_c rh}\partial_r\left(rh\partial_r c\right), \tag{4.1}$$

and the advective term is

$$\bar{u}\partial_r c. \tag{4.2}$$

The corresponding terms for the fluorescein are similar. Fig. 6 shows plots of diffusive and advective terms for our standard conditions with $r_w = 0.5$ and the Gaussian evaporation profile. It is clear from the plot that the diffusion term is always larger in magnitude than the advective term in the vicinity of TBU. We note that in this case, the diffusive term is not small near $r = 0$ at shorter times, but decreases there as time increases. Flow is toward the TBU region because capillary forces set up a pressure gradient where low pressure occurs in the TBU region. Near the edge of TBU, the flow toward TBU indicated by the advective terms carries osmolarity and fluorescein toward TBU, but they diffuse out from this region. The diffusion of fluorescein is smaller at earlier times but similar to osmolarity at later times; advection of fluorescein is always significantly larger than for osmolarity.

For smaller spot sizes, the dynamics are similar. For c, the diffusive transport is larger for any spot sizes for which we computed solutions. However, the diffusive term for the osmolarity remains at elevated values near $r = 0$ for increasingly longer time interval as r_w is decreased. For f, the increase around $r = 0$ is more pronounced and lasts longer as r_w is decreased, which indicates a more important role for advection for that solute.
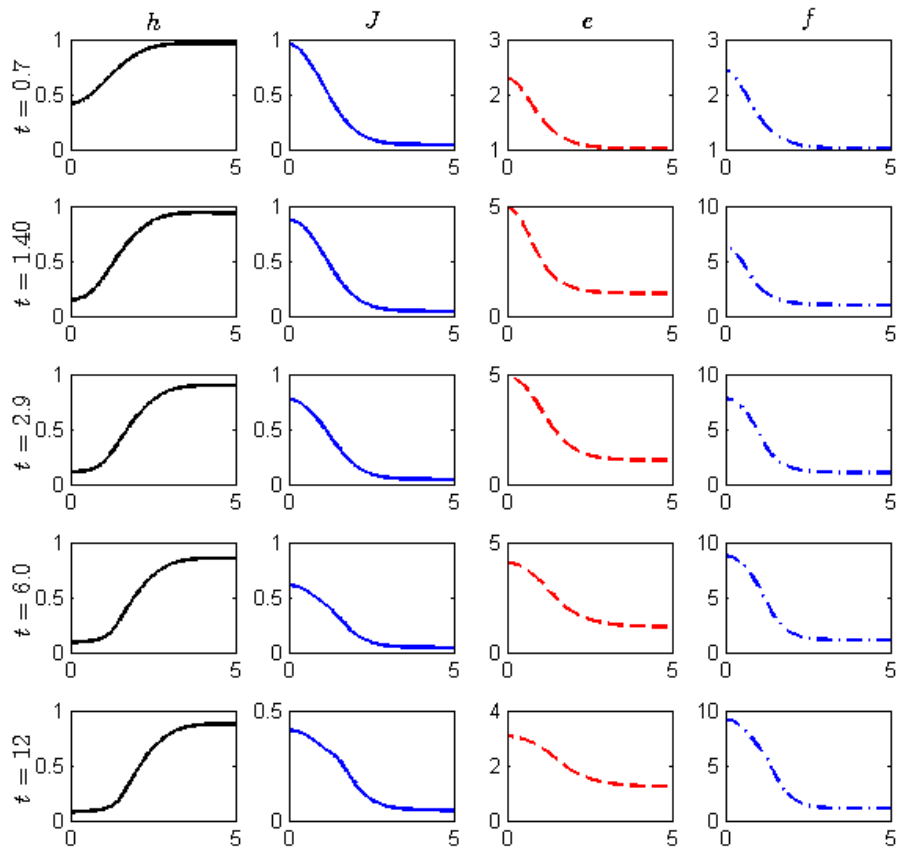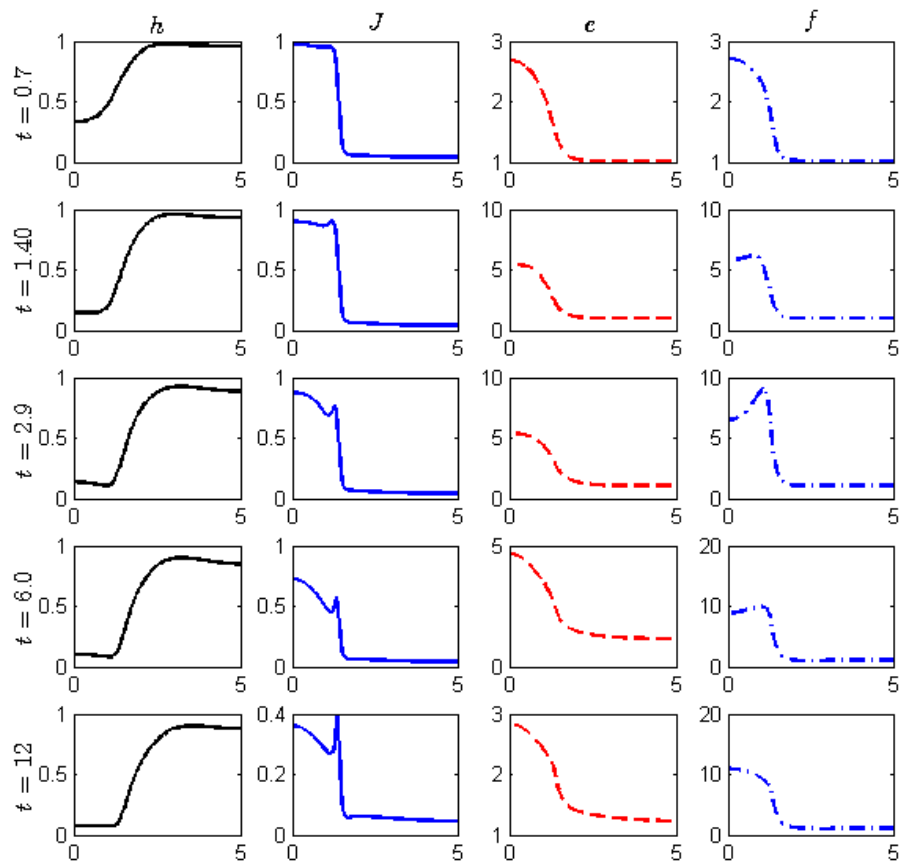
FIG. 4: From left to right in each column: thickness h, evaporation rate J, osmolarity c and FL concentration f at several times for a Gaussian J_f with $r_w = 1$, $v_0 = 20\mu$m/min and $d = 3.5\mu$m.

FIG. 5: From left to right in each column: thickness h, evporation rate J, osmolarity c and FL concentration f at several times for a tanh J_f with $r_w = 1.41$, $v_0 = 20\mu$m/min and $d = 3.5\mu$m.
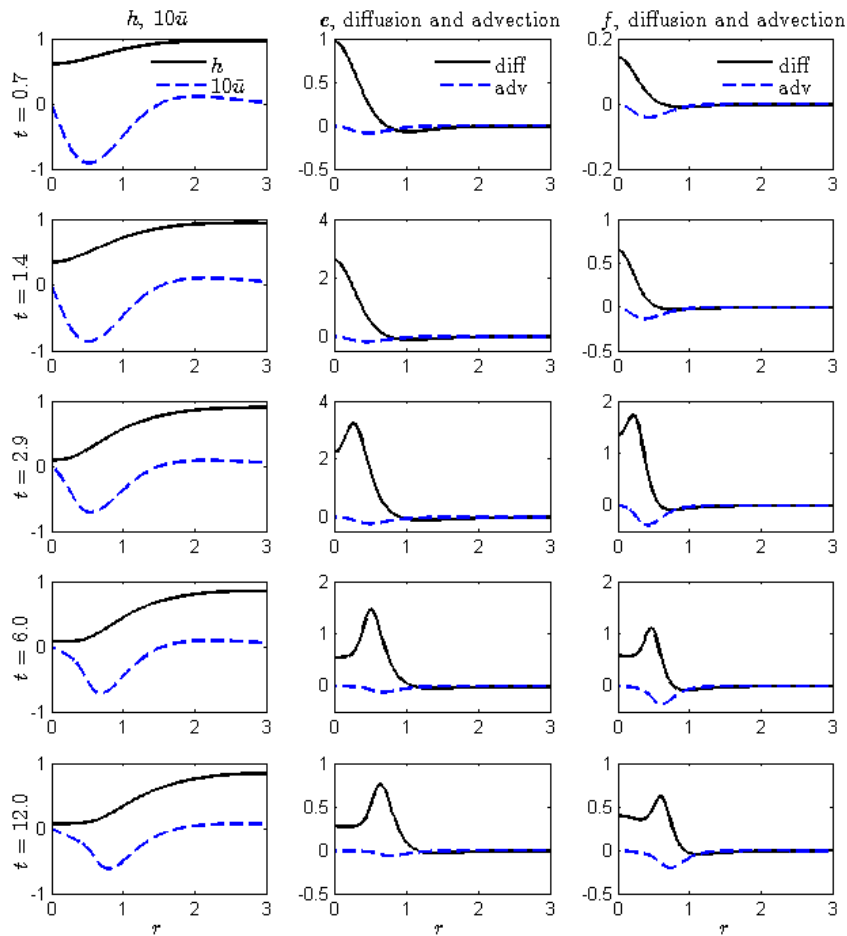
FIG. 6: Left column: plots of $h(r,t)$ and $\bar{u}(r,t)$ at several times. Middle column: plots of the diffusive term and the advective term for the osmolarity c at several times. Right column: diffusive and advective terms for the fluorescein concentration f at several times. This is the medium-sized Gaussian spot case for $r_w = 0.5$.

4.1.3 *Distribution of solutes* In this subsection, we plot the products *ch* and *fh*, from which we see that there is significant deviation from the mass conservation expression that holds in the flat film case. For the osmolarity, the flat film case would require that *ch* = 1 at all times for our initial conditions. For the FL concentration, $fh = f_0$ at all times in the flat film case (Braun et al., 2014).

Fig. 7 show the dynamics of *ch* and *fh* as functions of *r* at several times for two different spot sizes of increased evaporation. For $r_w = 1$ (top row), *ch* decreases in the TBU region because diffusion of solute out of these regions lowers the concentration compared to the flat film case. In this case the diffusion dominates because flow in the film is quite small when *h* nears $h_{eq} = (A\alpha)^{1/3}$. The thinning stops above this value set by the wetting term, but by an unexpectedly small amount, because diffusion lowers the osmolarity in the TBU region in comparison to the flat film case.

For the moderate spot size such as $r_w = 0.5$ (bottom row, Fig. 7), we see that *ch* has a delayed, then steady, decrease in the thinning region. The situation for *fh* is more complex with an initial increase followed by a decrease in the center of the thinning region. At the edge of the thinning region, an outward diffusion flux encounters inward transport from flow, and a local maximum develops by $t = 2.9$, which persists for some time thereafter.

For small spot size e.g. $r_w = 0.25$ (not shown here), the TBU develops slowly compared to in vivo observations. In this case, *ch* increases for a substantial time, then decreases in the TBU region because diffusion is sufficiently fast to allow osmolarity to escape. For *fh*, it takes longer for the decrease to begin, and the majority of the computation has an increase of *fh* at the center of the thinning region, which only reaches TBU near $t = 10$.

These results suggest how the dynamics change for smaller spot size. Having summarized the spatial dependence of the solutions and the relative importance of the effects, we now turn to summarizing the findings with plots of central values and TBU times.

4.1.4 *Central values as functions of time* In this subsection, the central values at $r = 0$ are plotted for the different variables *h*, *c* and *f* for different spot sizes. The FL concentration is relative to the initial value to facilitate plotting; the same relative changes are achieved for different initial values. The initial condition for the osmolarity is always kept the same i.e. (isotonic, $c = 1$). The case shown in Fig. 8 uses the Gaussian evaporation distribution with $v_0 = 20\mu$m/min, background thinning rate of $v_1 = 1\mu$m/min and characteristic film thickness $d = 3.5\mu$m. The flat film case evaporating at the peak rate v_0 is shown for comparison and the time for the flat film to thin is roughly $d/v_0 \approx 10.5$s. The central thickness goes below the flat film equilibrium value where osmotic influx would balance evaporative efflux. The time to reach the equilibrium thickness with wetting forces is close to d/v_0 (unit time in the plot) for $r_w = 1$, but is longer for the smaller spot sizes. The response for two different solutes helps in clarifying some of the key features here. The diffusion mechanism of the osmolarity (simple salt ions) is four times faster compared to that of fluorescein (relatively large dianions). As a result, the osmolarity diffuses quickly enough that it never reaches or exceeds the flat film result; the tear film does not become as salty as this theoretical limit even in the presence of the capillarity driven flow into the TBU region (sometimes called "healing flow"). This diffusion of osmolarity prevents the tear film from stopping at the flat film equilibrium thickness set by osmosis. The FL concentration significantly exceeds the flat film result, in contrast to the osmolarity, and because of this the intensity observed may change regimes from the initial state as seen in the previous subsection. The lowering of the peak value of *c* by diffusion was observed by Peng et al. (2014), but was not quantified in the detail that we present here.

The tear film thins to smaller values than would be predicted for a film that is uniform in space. The axisymmetric geometry allows the solutes that make up the osmolarity to diffuse away from the TBU region fast enough that osmosis does not supply enough water to balance the evaporation there. Hence,

the van der Waals term arrests thinning and reduces evaporation. This is presumably an approximation for the strong wettability of the glycocalyx at the corneal surface. This result was suggested by Peng et al. (2014), though they used a different evaporation model. In their model, when both evaporation and wetting terms are present, the tear film stops thinning when thickness of the film is around 10nm. This extremely small value is much smaller than the glycocalyx. Our model allows us to control the stopping location, but it assumes that the glycocalyx and the corneal surface can be homogenized to a flat surfaces with uniform properties, as well as using a simpler evaporation model.

4.1.5 *Spot TBU times (TBUT)* In Fig. 9, we show TBUT as a function of spot size r_w for different peak thinning rates v_0. The TBUT is defined as when the tear film thickness reaches twice the wetting equilibrium thickness $h_{eq} = (A\alpha)^{1/3}$ where evaporation stops due to the balance with the wetting term. In Fig. 9, we use $h_{eq} = 0.25\mu$m, so the TBUT was taken to be when the tear film reached 0.5μm. This size was chosen because the mathematical equilibrium is only slowly approached, which artificially extends the TBUT. In these results, osmosis is active with $P_o = 12.1\mu$m/s permeability (Braun et al., 2015). The results show that for $r_w > 0.8$ and $v_0 \geqslant 10\mu$m/min, the TBUT is about one unit of time. This indicates that the time to get to TBU is about d/v_0 which is the time for a flat film to evaporate away. This is true for either the Gaussian or the tanh profile. The extrema for this case are illustrated by $r_w = 1$ in Fig. 8. If the peak thinning rate is small, such as $v_0 = 5\mu$m/min, then the thinning is so slow that the TBUT increases relative to unit time because there is sufficient time for relatively weak capillary flow to act.

In the range of $0.4 \leqslant r_w \leqslant 0.8$ and with $v_0 \geqslant 10\mu$m/min, the TBUT increases as r_w decreases. We call this range moderate spot sizes. In this regime, capillary flow is increasing which brings more fluid into the TBU region but osmolarity can still diffuse out rapidly enough that the peak value of c does not approach the flat film case. The extrema for this case are illustrated by $r_w = 0.5$ in Fig. 8. The tanh profile (dashed curves in Fig. 9) shows the TBUT increasing slightly faster as r_w decreases in this range, and one could use the range $0.5 \leqslant r_w \leqslant 0.8$ if desired.

Finally, in the range $r_w \leqslant 0.4$, the TBUT is very long compared to typical in vivo results. For example, with a Gaussian evaporation profile and $r_w = 0.25$, it takes more than six time units (corresponding to six d/v_0, or more than a minute) to reach TBU. The difference between some in vivo results and our calculations may in part come from the need for clinicians to qualitatively interpret the nature of dark spots' appearance in the tear film Guillon (2002); however, the dominant physical effects do change in this regime. The extrema in this case are shown in Fig. 8. This happens because capillary flow into the TBU region (healing flow) is fast relative to the diffusion of solutes out of the TBU region, and this does two things. It (1) supplies fluid to the region via capillarity-driven flow to slow thinning and (2) raises c to values near those achieved by the flat film case, which increases osmotic supply of fluid. These two contributions slow thinning dramatically, and suggest that a different mechanism is present in small TBU spots.

Besides affecting TBUT via flow and osmolarity distributions, these dynamics have important consequences for imaging the tear film from the distributions of f in TBU.
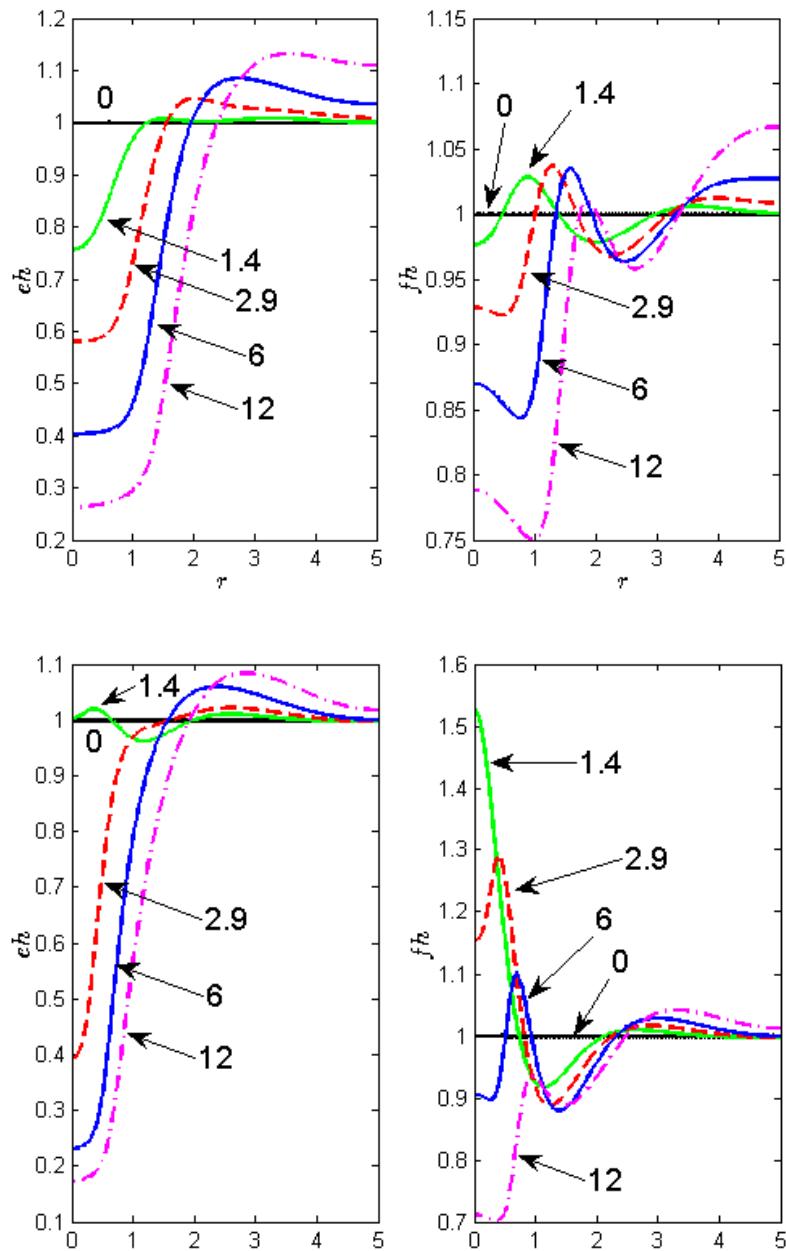
FIG. 7: The products ch (left) and fh (right) are shown for the nondimensional times indicated. For the upper row, the spot size is $r_w = 1$; for the lower row, $r_w = 0.5$. In all plots, with $v_0 = 20\mu$m/min, $v_1 = 1\mu$m/min and $d = 3.5\mu$m.
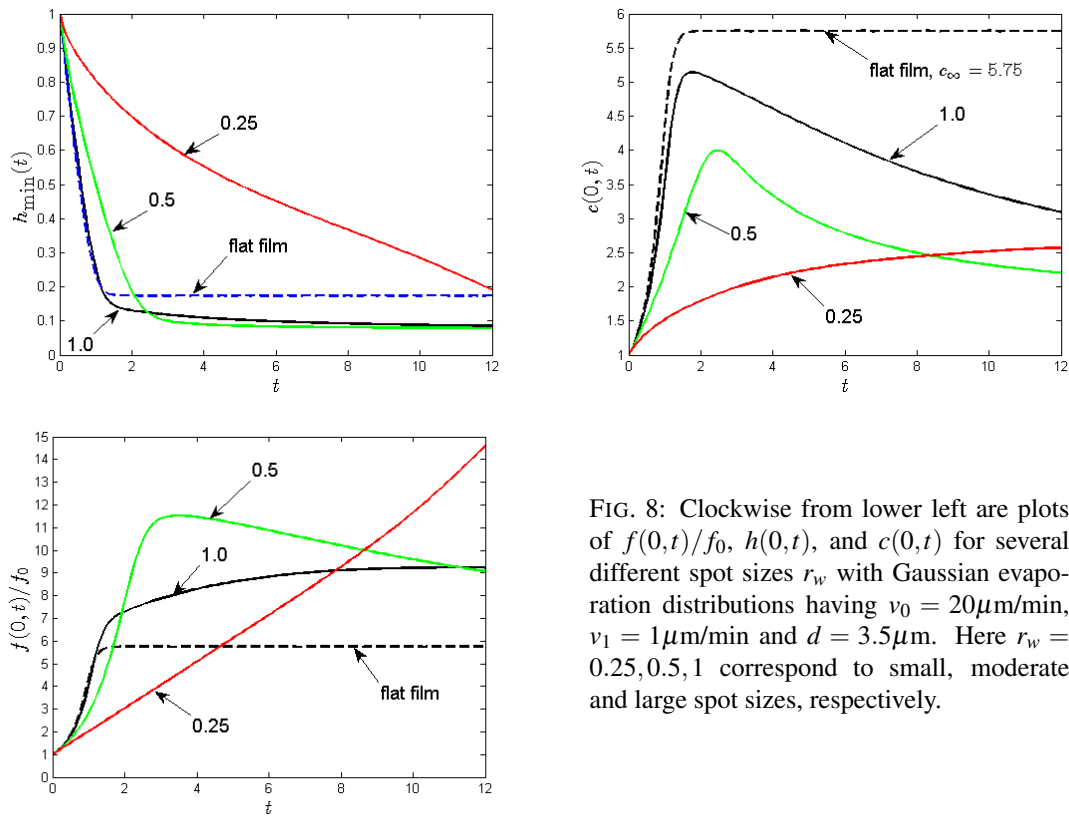
FIG. 8: Clockwise from lower left are plots of $f(0,t)/f_0$, $h(0,t)$, and $c(0,t)$ for several different spot sizes r_w with Gaussian evaporation distributions having $v_0 = 20\mu\text{m/min}$, $v_1 = 1\mu\text{m/min}$ and $d = 3.5\mu\text{m}$. Here $r_w = 0.25, 0.5, 1$ correspond to small, moderate and large spot sizes, respectively.

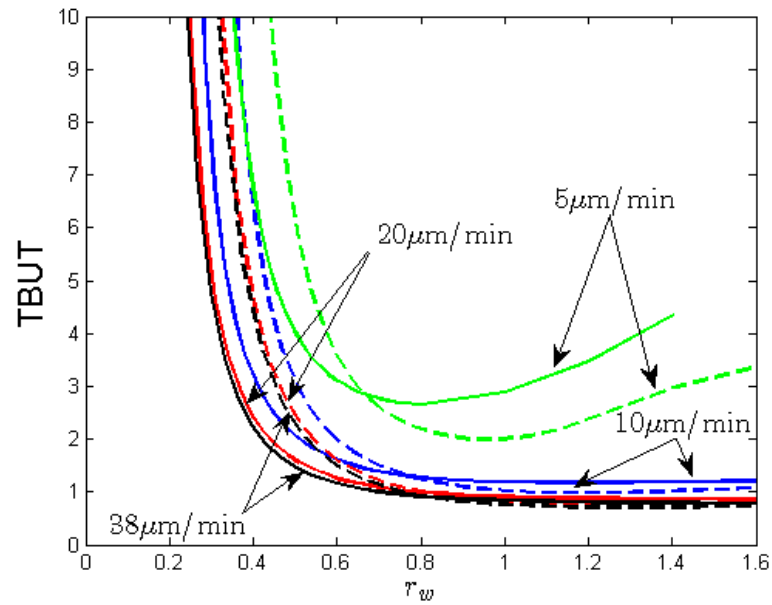R. J. Braun, T. A. Driscoll, C.G. Begley, P. E. King-Smith and J. I. Siddique

FIG. 9: TBUT for $d = 3.5\mu$m for four different maximum thinning rates v_0 (indicated) as function of the size of the evaporation distribution r_w. The solid curves are for the Gaussian distribution; dashed curves are the tanh distribution. The spot size is relative to the length scale ℓ.

4.1.6 *Intensity and thickness distributions*   Of considerable interest is the comparison between the actual thinning of the tear film and the estimated thinning that may be calculated from the fluorescent intensity pattern observed in vivo. Braun et al. (2015) studied an experimental result that used simultaneous imaging of FL and RI methods and compared thickness profiles from the intensity pattern. They found that the FL intensity pattern may be delayed compared to the actual thinning of the tear film, and that the TBU region was apparently narrower than that of the actual thinning region. In that work, the initial fluorescein concentration was fixed at the critical concentration of fluorescein (Webber and Jones, 1986; Nichols et al., 2012). This works well for the self-quenching regime (Nichols et al., 2012; Braun et al., 2014), but the initial concentration in vivo may be smaller even after concentrated solutions are instilled (Wu et al., 2015). This leads us to investigate both $a\sqrt{I}$ and a^2I as approximations for the TF thickness. Here a is a normalization constant chosen to match the intensity with the uniform initial thickness distribution. We now compare them for a range of initial concentrations f_0 and TBU spot sizes r_w. We begin with a representative time sequence of the relevant variables, then summarize the dependence over a range of parameters at certain representative times.

Figure 10 shows the intensity and thickness distributions for spot sizes close to, but before, TBU. In making these plots the time displayed depends on the spot size because the role of capillary-driven flow increases as the spot size decreases. We have chosen the end time of the calculation t_e so that the wetting terms are not important in slowing down the thinning. In the upper left column, there is a wide hole and a dilute f_0, so that little happens with a^2I or $a\sqrt{I}$ during thinning. For narrower widths, the intensity can increase in the streak, at least before f increases too much during thinning within the spot (not shown in this figure). In both of the first rows ($f_0 \leqslant 0.25$), there is little correlation between the intensity and the thickness up to these times. For initial concentrations in the third row, it is typical that intensity a^2I follows the thickness better than $a\sqrt{I}$. For $f_0 \geqslant 1$, the agreement becomes better for $a\sqrt{I}$ because the thinning of the tear film increases f firmly into the self-quenching regime. For the last three rows, the agreement is better for larger spot size (the first two columns).

4.1.7 *Intensity and osmolarity distributions*   As discussed by Nichols et al. (2012) and Braun et al. (2014), the use of the self-quenching of fluorescein can be used to estimate relative changes in the thickness of the tear film. For $f' > f_{cr}$, the thickness can be approximated by $a\sqrt{I}$ as discussed above. The assumptions that are typically used to to this included that the film is flat and spatially uniform. Under those conditions and assuming initially isotonic conditions ($c = 1$), mass conservation $hc = 1$ in our scalings. Thus, one may estimate the osmolarity after eliminating h so that $c = 1/(a\sqrt{I})$ or $1/(a^2I)$. This is clearly not the case in TBU because tangential flow is present; it is sensible to to try the approach in any case from a clinical point of view. We now examine what the model reveals on this point.

Figure 11 summarizes the intensity and solute distributions for spot sizes close to, but before, TBU. Again in this case, the time displayed depends on the spot size because the role of capillary-driven flow increases as the spot size decreases. Again, in both of the first rows the correlation between osmolarity and $1/(a^2I)$ is reasonably good. For $f_0 = 0.5$ and the larger spot sizes, the reciprocal of the intensity is a qualitative indicator of osmolarity; for $r_w = 0.25$, it is a poor indicator. However, below the third row or below where $f_0 > 0.50$, $1/(a^2I)$ is a relatively poor indicator of the osmolarity for all spot sizes.
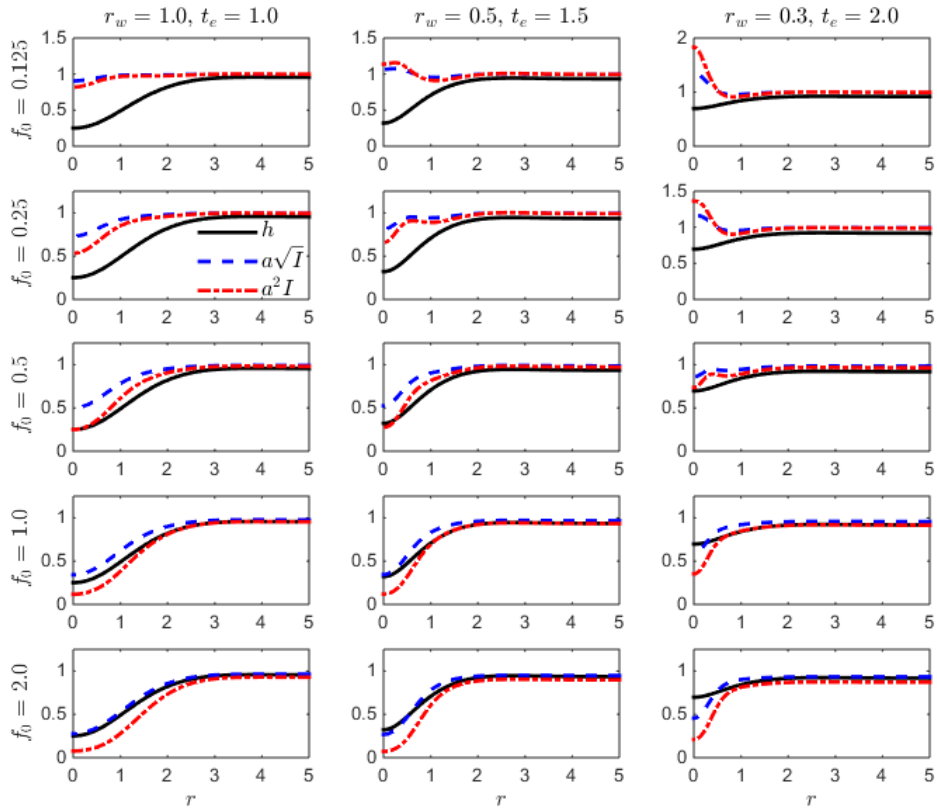
FIG. 10: Distribution of h, $a^2 I$, and $a\sqrt{I}$ at times before TBU for initial thickness $d = 3.5\mu$m for three different spot sizes r_w and five different initial fluorescein concentrations ($f_0 = 1$ is the critical concentration). Here r_w is normalized with $\ell = 0.35$mm and t_e is the end time normalized with d/v_0. The dash-dot curve is the fluorescent intensity I and the dashed curve is its square root $a\sqrt{I}$; both are normalized to unity for the intial flat film thickenss for comparison with the computed thickness which is normalized with d.
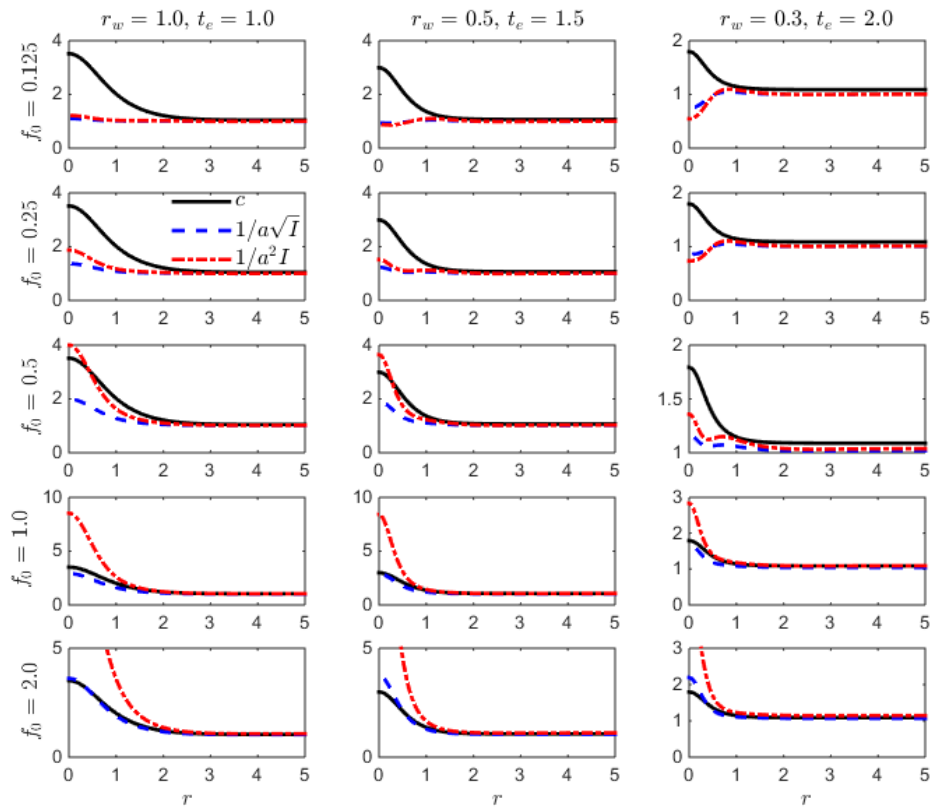
FIG. 11: Distribution of c, $1/(a^2 I)$, and $1/(a\sqrt{I})$ at times before TBU for initial thickness $d = 3.5\mu$m for three different spot sizes r_w and five different initial fluorescein concentrations. The dash-dot curve is $1/(a^2 I)$ and the dashed curve is its square root $1/(a\sqrt{I})$; both are normalized to unity for the initial flat film thickenss for comparison with the computed osmolarity which is normalized with $c_0 = 300$mOsM.

4.2 *Streaks*

The equations for streaks are given in Appendix C. Overall the dynamics for streaks are similar to those for spots; we show summary cases for comparison in this section. Unless otherwise indicated, the parameters are the same as in the section for spots.

4.2.1 *TBUT for streaks* The TBUT is calculated by finding when the tear film thickness reaches twice the wetting equilibrium thickness $h_{eq} = 0.25\mu$m where evaporation stops, or 0.5μm. This size was chosen because the mathematical equilibrium is only slowly approached, which artificially extends the TBUT.
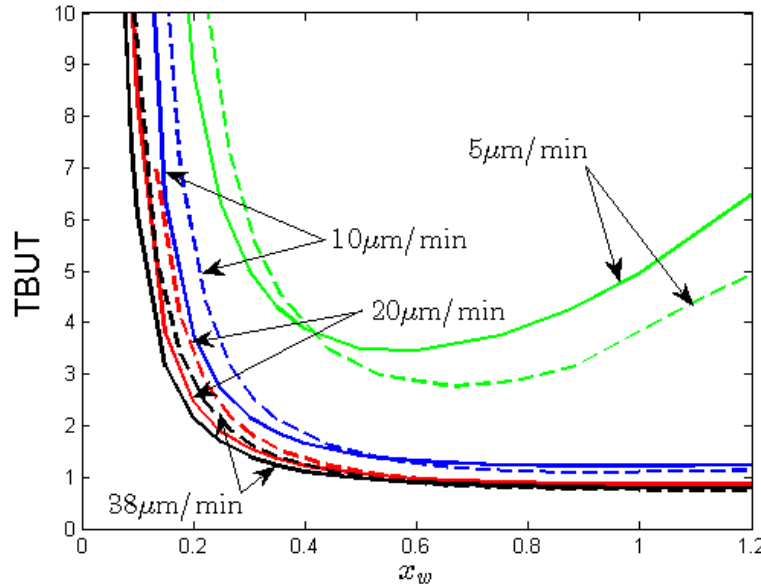

FIG. 12: TBUT for $d = 3.5\mu$m for four different maximum thinning rates v_0 (indicated) as a function of the width of the evaporation distribution x_w that leads to streak TBU. The solid curves are for the Gaussian distribution; dashed curves are the tanh distribution.

Following the categorization of spots using TBUT, we can classify streak widths as follows. For $x_w \leqslant 0.25$, we have small (narrow) streaks; in this case, TBUT is too long for physiological times because capillary flow slows down the process. For $0.25 < x_w \leqslant 0.6$, we have moderately wide streaks. In this case, diffusion of osomlarity and capillary flow are both important and start to increase the TBUT. For $0.6 < x_w$, we have large (wide) streaks, where evaporation and diffusion of osmolarity compete but the model still predicts TBU in approximately d/v_0 time.

4.2.2 *Central values of thickness and solutes vs flat films* In this subsection, the central values at $x = 0$ are plotted for the different variables h, c and f for different peak evaporation rates in a Gaussian distribution and different streak widths. The FL concentration is relative to the initial value to facilitate plotting; the same relative changes are achieved for different initial values. The osmolarity always

has the same initial condition (isotonic, $c = 1$). The first case has a Gaussian evaporation distribution $v_0 = 20\mu$m/min with background rate is $v_1 = 1\mu$m/min and characteristic film thickness $d = 3.5\mu$m. The flat film case evaporating at the peak rate v_0 is shown for comparison. The time for the flat film to
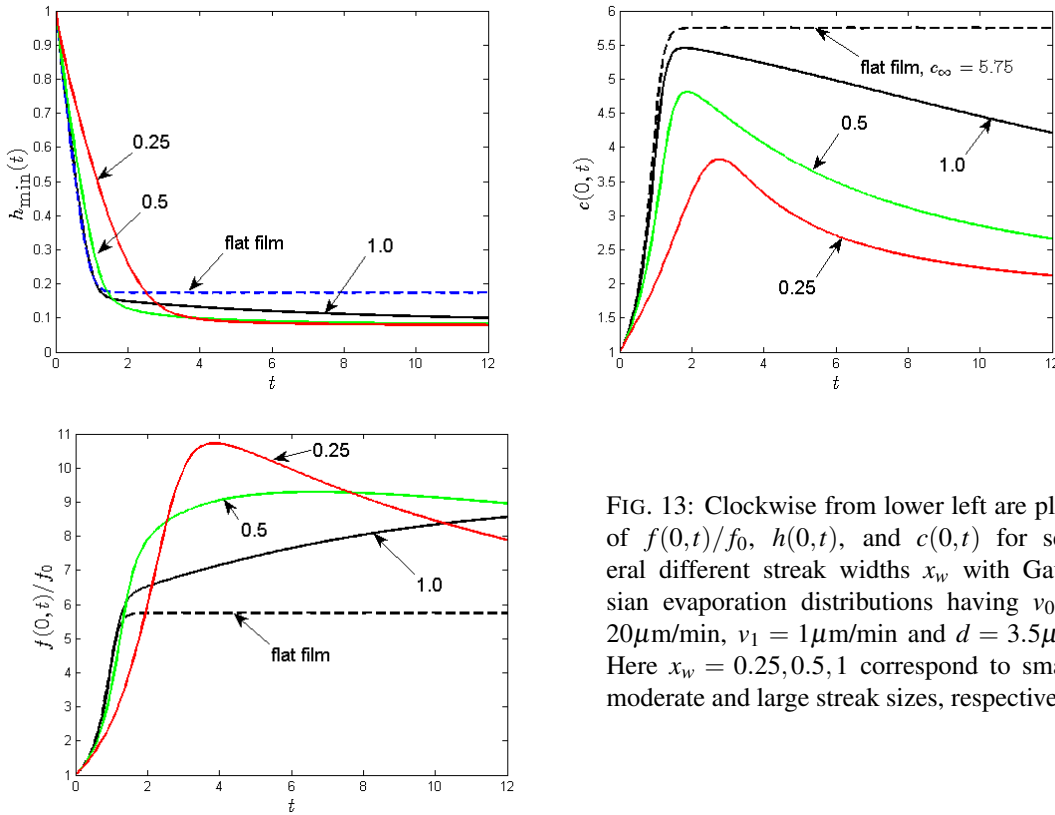

FIG. 13: Clockwise from lower left are plots of $f(0,t)/f_0$, $h(0,t)$, and $c(0,t)$ for several different streak widths x_w with Gaussian evaporation distributions having $v_0 = 20\mu$m/min, $v_1 = 1\mu$m/min and $d = 3.5\mu$m. Here $x_w = 0.25, 0.5, 1$ correspond to small, moderate and large streak sizes, respectively.

thin is roughly $d/v_0 \approx 10.5$s. The central thickness goes below the flat film equilibrium where osmotic influx would balance evaporative efflux. The time to approach the equilibrium thickness with wetting forces is close to d/v_0 (unit time in the plot) for $x_w = 1$ and 0.5, but is longer for the smaller streak width $x_w = 0.25$.

For wider streaks, the maximum c approaches the flat film values but as x_w is decreased, the maximum c is decreased and the time when it is reached is increased. The increased importance of diffusion from increased gradients in narrower streaks is responsible for the decreased peak value. The flourescein concentration peaks later than for the osmolarity for wider streaks. As x_w decreases, the peak value of f increases and occurs at earlier times due to the stronger capillary flow together with less diffusion of f compared to c. The peak values of f for streaks are smaller than for spots. The time scale of decrease of solutes after the peak values is set by the diffusion of solute out of the TBU region, and this part of the dynamics occurs after h has decreased to values below the flat film limit. If one were to compute for very long times (well beyond physiological values), the wetting term would balance the evaporation term and stop thinning.

4.2.3   *Intensity and thickness distributions*   Figure 14 summarizes the intensity and thickness distributions for streaks close to, but before, TBU. The final time displayed (t_e) depends on the streak width because the capillary-driven flow into the TBU region increases as the streak width decreases. The time
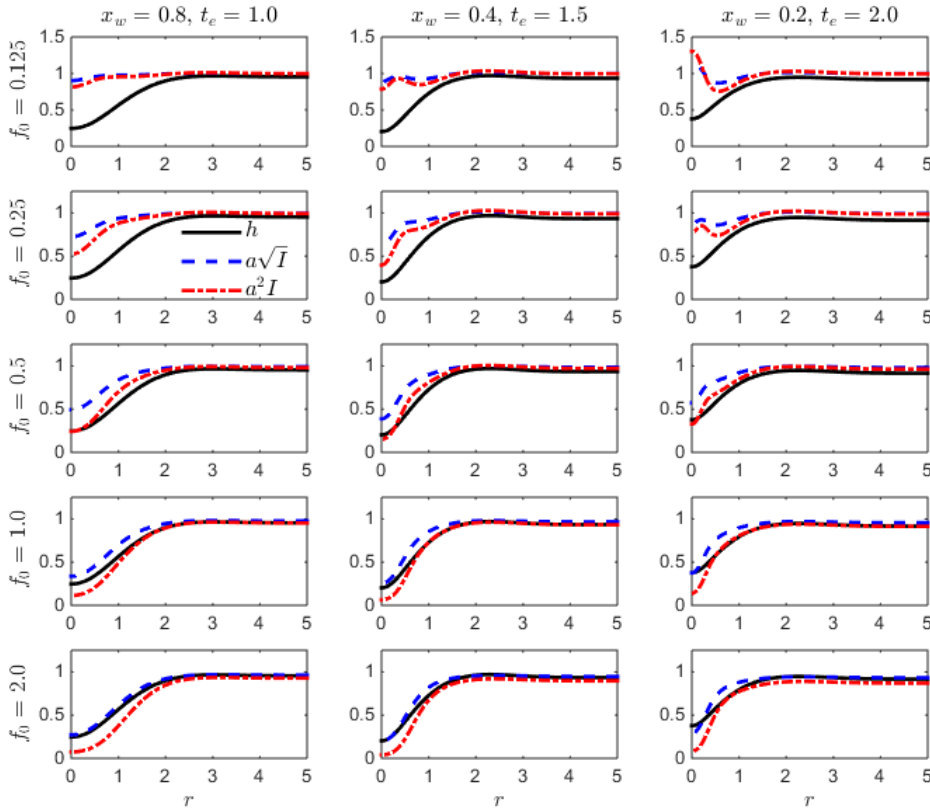

FIG. 14: Distribution of h, $a^2 I$, and $a\sqrt{I}$ at times before TBU for initial thickness $d = 3.5\mu$m for three different streak widths x_m and five different initial fluorescein concentrations ($f_0 = 1$ is the critical concentration). Here x_w is normalized with $\ell = 0.35$mm and t_e is the end time normalized with d/v_0. The dash-dot curve is the fluorescent intensity $a^2 I$ and the dashed curve is its square root $a\sqrt{I}$; both are normalized to unity for the initial flat film thickness for comparison with the computed thickness which is normalized with d.

is chosen so that the wetting terms are not yet important in slowing thinning. In the upper left, we have a wide hole and a dilute f, so that little happens with $a^2 I$ or $a\sqrt{I}$ during thinning. For narrower widths, the intensity can increase in the streak, at least before f increases too much during thinning in the streak (not shown in this figure). In both of the first rows ($f_0 \leqslant 0.25$), there is little correlation between the intensity and the thickness up to these times. For initial concentrations in the third row, it is typical that intensity $a^2 I$ follows the thickness better than $a\sqrt{I}$. For $f_0 \geqslant 1$, the agreement between h and $a\sqrt{I}$

improves because the thinning of the tear film is increasing f firmly into the self-quenching regime.

5. Discussion

The capillary-driven flow carries solutes toward the TBU region, but elevated levels there cause Fickian diffusion out of the TBU region. The size of the Peclet number for the simple ions included in the osmolarity is such that diffusion is more important than advection; the diffusion term is shown to dominate the advection term in Section 4.1.2. As a result, the peak values of osmolarity in the TBU region are lower than for similar conditions in a flat, spatially-uniform film (Section 4.1.4). Furthermore, the tear film doesn't stop thinning at the same thickness as would be computed by a spatially-uniform flat film model because the osmolarity diffuses out of the TBU region. The lowered peak value prevents the osmotic supply from balancing the loss of water due to evaporation. These results are consistent with Peng et al. (2014) and Braun et al. (2015). On the other hand, the Peclet number for fluorescein is about four times larger, the increased advection affects the fluorescein transport and this causes peak values of that concentration to easily exceed that of the flat film under many conditions. The peak values of FL in the TBU region are always larger than for the osmolarity for the cases shown here. Because advection is increased in FL transport, the FL distribution is narrower than or comparable to that for the osmolarity as well.

To investigate the redistribution of the solutes compared to the flat film case, we plotted the distribution of mass given ch and fh. Results from Fig. 7 show significant deviation from the mass conservation for the flat film, and this was seen in all cases. The way the deviation occurs varies depending on the hole size and the time during the simulation. The complex dynamics of these quantities typically show an increase in the mass at the center of the developing TBU region at early times, then a decrease inside the TBU region at later times once diffusion has had time to redistribute the solutes. The increase is larger and lasts longer for the fluorescein concentration.

The length scale ℓ is the length where surface tension and viscous forces in the film balance; for spots that are significantly smaller than ℓ, the capillary-pressure-driven local flow is dominant in the TBU region causing reduced thinning rates and longer TBU times. This result agrees with previous works (Peng et al., 2014; Braun et al., 2015), but the current work quantifies when this occurs in parameter space and gives a more complete picture of the dynamics. In particular, we were able to summarize the TBUT for spots or streaks with respect to size and thinning (evaporation) rate (Figure 9). In doing this, it is clear that evaporation can drive TBU at physiologically reasonable times when the size of TBU is around $\ell/2$ or larger. For smaller sizes, it is likely that another mechanism is responsible. For comparable amounts of evaporation, the results were not very sensitive to the details of the evaporation for the Gaussian and tanh profiles that we studied.

The dynamics of the thickness and FL intensity were compared in some detail. The FL intensity distribution $I(x,t)$ is slower to develop than a thin region for small small and for short times. For longer times, the FL intensity dynamics seemed to evolve faster than the thickness. The difference in dynamics between h and I were minimized for spot sizes comparable to ℓ or larger. The capillary-driven flow that transports f affects the imaging of the TBU process as well. The narrower distribution of the fluorescein concentration leads to an FL intensity distribution that is narrower than the actual thickness distribution. This was seen in both spots and streaks. The effect of the mass redistribution on estimating the thickness and osmolarity distributions was summarized in Figures 10, 11, and 14. Considering the thickness estimation, the visualized TBU region from the quenching regime is narrower than the actual thickness distribution. This has been observed in vivo from the results shown here (Figures 2 and 3) and in Braun et al. (2015).

It is reasonable to try to estimate the osmolarity from the FL intensity distribution, under the assumption that the intensity gives information about the fluorescein concentration. In the past, efforts to do this have assumed that the osmolarity and fluorescein are transported in an equivalent manner inside the tear film. As we have shown here, the fluorescein concentration is affected more by the flow inside the tear film and much more so than the osmolarity. Thus, estimating the osmolarity from the intensity distribution should be done with care, and is likely to only be qualitative at best.

Variation of the initial FL concentration shows complicated dynamics which changes with spot or streak size; the results are in Sections 4.1.7 and 4.2.3. In the clinic or in basic science, one rarely operates much below the critical concentration though experiments may start there (Wu et al., 2015). If one started an experiment in the dilute regime, then it is possible that TBU regions could brighten significantly because of inward flow toward TBU together with evaporation and then subsequently darken via FL self-quenching. This may make consistent interpretation of imaging difficult in this concentration range, particularly for small spots and streaks as shown in the upper left corners of Figs. 10 and 14. When beginning observations at the critical concentration or larger, there is no such ambiguity (Braun et al., 2014).

6. Conclusions and Future Directions

This paper explored the consequences of localized evaporation for the tear film thickness, solute transport and FL imaging. The model used a scaling that clarified when the TBU mechanism may be driven by evaporation. In that case, capillarity balances viscous effects, or is dominated by them. In the case when capillarity dominates for small enough spots or narrow enough streaks, another mechanism is required. We are currently studying a Marangoni-driven model of TBU that appears to fit the experimental evidence for many small spots and narrow streaks.

The model found that solute transport was important in TBU. The osmolarity redistribution due to diffusion promoted TBU as been found previously (Peng et al., 2014; Braun et al., 2015), and that peak values of osmolarity are lowered from what would be obtained in the flat film case. The computation of the fluorescein concentration distribution revealed that it is more strongly affected by advection, and that its peak values exceeded those found from flat film models. The imaging of the tear film from FL intensity is complicated by the advective transport, making TBU images appear to be narrower than those from direct imaging of the tear film thickness. The estimation of the tear film thickness was also complicated as well, moreso than in the flat film case as discussed in Braun et al. (2014). Knowledge of the fluorescein concentration at the start of the FL intensity experiments is very helpful for interpreting the observations (Braun et al., 2014; Wu et al., 2015).

The model problems in this paper use specified evaporation rate distributions, which is a vast simplification of the actual lipid layer. While this appears to accurately reflect some carefully controlled experiments in the clinic (King-Smith, Reuter, Braun, Nichols and Nichols, 2013, e.g., their Fig. 6), having a dynamic lipid layer atop the aqueous layer and an evaporation rate that depends on the lipid layer thickness as well as environmental conditions (Peng et al., 2014, e.g.) would be a step closer to in vivo situations in a wider range of environments. Such a model may also be better able to describe the spreading of TBU after its onset. Two dimensional TBU computations would be of significant value for comparison with experiment as well. A much bigger step would include the dynamics of blinking on the lipid layer as well as TBU dynamics.

Acknowledgments

References

Baudouin, C., Aragona, P., Messmer, E. M., Tomlinson, A., Calonge, M., Boboridis, K. G., Akova, Y. A., Geerling, G., Labetoulle, M. and Rolando, M. (2013), 'Role of hyperosmolarity in the pathogenesis and management of dry eye disease: Proceedings of the OCEAN group meeting', *Ocul. Surf.* **11**, 246–258.

Begley, C. G., Simpson, T., Liu, H., Salvo, E., Wu, Z., Bradley, A. and Situ, P. (2013), 'Quantative analysis of tear film fluorescence and discomfort during tear film instability and thinning', *Invest. Ophthalmol. Vis. Sci.* **54**, 26452653.

Benedetto, D. A., Clinch, T. E. and Laibson, P. R. (1986), 'In vivo observations of tear dynamics using fluorophotometry', *Arch. Ophthalmol.* **102**, 410–412.

Berger, R. E. and Corrsin, S. (1974), 'A surface tension gradient mechanism for driving the pre-corneal tear film after a blink', *J. Biomech.* **7**, 225–238.

Braun, R. J. (2012), 'Dynamics of the tear film', *Annu. Rev. Fluid Mech.* **44**, 267–297.

Braun, R. J., Gewecke, N., Begley, C. G., King-Smith, P. E. and Siddique, J. I. (2014), 'A model for tear film thinning with osmolarity and fluorescein', *Invest. Ophthalmol. Vis. Sci.* **55**, 1133–1142.

Braun, R. J., King-Smith, P. E., Begley, C. G., Li, L. and Gewecke, N. R. (2015), 'Dynamics and function of the tear film in relation to the blink cycle.', *Prog. Retin. Eye Res.* **45**, 132–164.

Braun, R. J., Usha, R., McFadden, G. B., Driscoll, T. A., Cook, L. P. and King-Smith, P. E. (2012), 'Thin film dynamics on a prolate spheroid with application to the cornea', *J. Eng. Math.* **73**, 121–138.

Bron, A., Argüeso, P., Irkec, M. and Bright, F. V. (2015), 'Clinical staining of the ocular surface: Mechanisms and interpretations', *Prog. Ret. Eye Res.* **78**, 36–61.

Bron, A., Tiffany, J., Gouveia, S., Yokoi, N. and Voon, L. (2004), 'Functional aspects of the tear film lipid layer', *Exp. Eye Res.* **78**, 347–360.

Carlson, N. B. and Kurtz, D. (2004), *Clinical Procedures for Ocular Examination*, 3rd edn, McGraw Hill, New York.

Casalini, T., Salvalaglio, M., Perale, G., Masi, M. and Cavallotti, C. (2011), 'Diffusion and aggregation of sodium fluorescein in aqueous solutions', *J. Phys. Chem. B* **115**, 12896–12904.

Cerretani, C. F. and Radke, C. J. (2014), 'Tear dynamics in healthy and dry eyes', *Curr. Eye Res.* **39**, 580–595.

Craster, R. V. and Matar, O. K. (2009), 'Dynamics and stability of thin liquid films', *Rev. Mod. Phys.* **81**, 1131–1198.

Dartt, D. A. and Willcox, M. D. P. (2013), 'Complexity of the tear film: Importance in homeostasis and dysfunction during disease', *Exp. Eye Res.* **117**, 1–3.

Doane, M. (1989), 'An instrument for in vivo tear film interferometry', *Optom. Vis. Sci.* **66**, 383–388.

Doane, M. G. (1981), 'Blinking and the mechanics of the lacrimal drainage system', *Ophthalmology* **88**, 844–851.

Gilbard, J. P., Farris, R. L. and Santamaria, J. (1978), 'Osmolarity of tear microvolumes in keratocon-junctivitis sicca', *Arch. Ophthalmol.* **96**, 677–681.

Gipson, I. K. (2004), 'Distribution of mucins at the ocular surface', *Exp. Eye Res.* **78**, 379–388.

Goto, E. and Tseng, S. C. G. (2003), 'Kinetic analysis of tear interference images in aqueous tear deficiency dry eye before and after punctal occlusion', *Invest. Ophthalmol. Vis. Sci.* **44**, 1897–1905.

Govindarajan, B. and Gipson, I. (2010), 'Membrane-tethered mucins have multiple functions on the ocular surface', *Exp. Eye Res.* **90**, 655–693.

Guillon, J.-P. (2002), Current clinical techniques to study the tear film and tear secretions, *in* D. R. Korb, J. Craig, M. Doughty, J.-P. Guillon, G. Smith and A. Tomlinson, eds, 'The Tear Film: Structure, function and clinical examination', Butterworth-Heinemann, pp. 51–81.

Himebaugh, N., Wright, A. R., Bradley, A., Begley, C. G. and Thibos, L. N. (2003), 'Use of retroillu-mination to visualize optical aberrations caused by tear film break-up', *Optom. Vis. Sci.* **80**, 69–78.

Holly, F. (1973), 'Formation and rupture of the tear film', *Exp. Eye Res.* **15**, 515–525.

Jensen, O. E. and Grotberg, J. B. (1993), 'The spreading of heat or soluble surfactant along a thin liquid film', *Phys. Fluids A* **75**, 58–68.

Kimball, S. H., King-Smith, P. E. and Nichols, J. J. (2010), 'Evidence for the major contribution of evaporation to tear film thinning between blinks', *Invest. Opthalmol. Vis. Sci.* **51**, 6294–6297.

King-Smith, P. E., Fink, B. A., Hill, R. M., Koelling, K. W. and Tiffany, J. M. (2004), 'The thickness of the tear film', *Curr. Eye. Res.* **29**, 357–368.

King-Smith, P. E., Fink, B. A., Nichols, J. J., Nichols, K. K., Braun, R. J. and McFadden, G. B. (2009), 'The contribution of lipid layer movement to tear film thinning and breakup', *Invest. Ophthalmol. Visual Sci.* **50**, 2747–2756.

King-Smith, P. E., Hinel, E. A. and Nichols, J. J. (2010), 'Application of a novel interferometric method to investigate the relation between lipid layer thickness and tear film thinning', *Invest. Ophthalmol. Vis. Sci.* **51**, 2418–23.

King-Smith, P. E., Nichols, J. J., Nichols, K. K. and Braun, R. J. (2011), 'A high resolution microscope for imaging the lipid layer of the tear film', *Ocular Surf.* **9**(4), 197–211.

King-Smith, P. E., Ramamoorthy, P., Braun, R. J. and Nichols, J. J. (2013), 'Tear film images and breakup analyzed using fluorescent quenching', *Invest. Ophthalmol. Vis. Sci.* **54**, 6003–6011.

King-Smith, P. E., Reuter, K. S., Braun, R. J., Nichols, J. J. and Nichols, K. K. (2013), 'Tear film breakup and structure studied by simultaneous video recording of fluorescence and tear film lipid layer, TFLL, images', *Invest. Ophthalmol. Vis. Sci.* **54**, 4900–4909.

Lakowicz, J. R. (2006), *Principles of Fluorescence Spectroscopy*, 3rd edn, Springer, New York.

Lemp, M. A., Bron, A. J., Baudoin, C., Benitez Del Castillo, J. M., Geffen, D., Tauber, J., Foulks, G. N., Pepose, J. S. and Sullivan, B. D. (2011), 'Tear osmolarity in the diagnosis and management of dry eye disease', *Am. J. Ophthalmol.* **151**, 792–798.

Lemp, M. A. et al. (2007), 'The definition and classification of dry eye disease: Report of the Definition and Classification Subcommittee of the International Dry Eye WorkShop', *Ocul. Surf.* **5**, 75–92.

Li, L. and Braun, R. J. (2012), 'A model for the human tear film with heating from within the eye', *Phys. Fluids* **24**, 062103.

Li, L., Braun, R. J., Driscoll, T. A., Henshaw, W. D., Banks, J. W. and King-Smith, P. E. (2015), 'Computed tear film and osmolarity dynamics on an eye-shaped domain', *Math. Med. Biol.* **10**, 1–35.

Li, L., Braun, R. J., Maki, K. L., Henshaw, W. D. and King-Smith, P. E. (2014), 'Tear film dynamics with evaporation, wetting and time-dependent flux boundary condition on an eye-shaped domain', *Phys. Fluids* **26**, 052101.

Liu, H., Begley, C. G., Chalmers, R., Wilson, G., Srinivas, S. P. and Wilkinson, J. A. (2006), 'A link between tear instability and hyperosmolarity in dry eye', *Optom. Vis. Sci.* **83**, 723–730.

Liu, H., Begley, C. G., Chen, M., Bradley, A., Bonanno, J., McNamara, N. A., Nelson, J. D. and Simpson, T. (2009), 'A link between tear instability and hyperosmolarity in dry eye', *Invest. Ophthalmol. Vis. Sci.* **50**, 3671–3679.

Maki, K. L., Braun, R. J., Henshaw, W. D. and King-Smith, P. E. (2010), 'Tear film dynamics on an eye-shaped domain I: pressure boundary conditions', *Math. Med. Biol.* **27**, 227–254.

Maki, K. L., Braun, R. J., Ucciferro, P., Henshaw, W. D. and King-Smith, P. E. (2010), 'Tear film dynamics on an eye-shaped domain. Part 2. Flux boundary conditions', *J. Fluid Mech.* **647**, 361–390.

Matar, O. K., Craster, R. V. and Warner, M. R. E. (2002), 'Surfactant transport on highly viscous surface films', *J. Fluid Mech.* **466**, 85–111.

Miller, K. L., Polse, K. A. and Radke, C. J. (2002), 'Black line formation and the "perched" human tear film', *Curr. Eye Res.* **25**, 155–162.

Mishima, S. and Maurice, D. (1961), 'The oily layer of the tear film and evaporation from the corneal surface', *Exp. Eye Res.* **1**, 39–45.

Montés-Micó, R., Cervino, A., Ferrer-Blasco, T., Garca-Lázaro, S. and Madrid-Costa, D. (2010), 'The tear film and the optical quality of the eye', *The Ocular Surface* **8**(4), 185–192.

Mota, M. C., Carvalho, P., Ramalho, J. and Leite, E. (1991), 'Spectrophotometric analysis of sodium fluorescein aqueous solutions. determination of molar absorption coefficient', *Int. Ophthalmol.* **15**, 321–326.

Nagyová, B. and Tiffany, J. M. (1999), 'Components of tears responsible for surface tension', *Curr. Eye Res.* **19**, 4–11.

Nichols, J. J., King-Smith, P. E., Hinel, E. A., Thangavelu, M., and Nichols, K. K. (2012), 'The use of fluorescent quenching in studying the contribution of evaporation to tear thinning', *Invest. Ophthalmol. Vis. Sci.* **53**, 5426–5432.

Nichols, J. J., Mitchell, G. L. and King-Smith, P. E. (2005), 'Thinning rate of the precorneal and prelens tear films', *Invest. Ophthalmol. Visual Sci.* **46**, 2353–2361.

Norn, M. S. (1969), 'Dessication of the precorneal film I. corneal wetting time', *Acta Ophthalmol.* **4**, 865–880.

Norn, M. S. (1979), 'Semiquantitative interference study of the fatty layer of precorneal film', *Acta Ophthalmol.* **57**, 766–774.

Pandit, J. C., Nagyová, B., Bron, A. J. and Tiffany, J. M. (1999), 'Physical properties of stimulated and unstimulated tears', *Exp. Eye Res.* **68**, 247–53.

Peng, C.-C., Cerretani, C., Braun, R. J. and Radke, C. J. (2014), 'Evaporation-driven instability of the precorneal tear film', *Adv. Coll. Interface Sci.* **206**, 250–264.

Riquelme, R., Lira, I., Pérez-López, C., Rayas, J. A. and Rodrguez-Vera, R. (2007), 'Interferometric measurement of a diffusion coefficient: comparison of two methods and uncertainty analysis', *J. Phys. D. Appl. Phys.* **40**, 2769–2776.

Sharma, A. and Ruckenstein, E. (1985), 'Mechanism of tear film rupture and formation of dry spots on cornea', *J. Coll. Interface Sci.* **106**, 12–27.

Sharma, A. and Ruckenstein, E. (1986*a*), 'An analytical nonlinear theory of thin film rupture and its application to wetting films', *J. Coll. Interface Sci.* **113**, 8–34.

Sharma, A. and Ruckenstein, E. (1986*b*), 'The role of lipid abnormalities, aqueous and mucus deficiencies in the tear film breakup, and implications for tear substitutes and contact lens tolerance', *J. Coll. Interface Sci.* **111**, 456–479.

Smith, G. D. (1996), *Numerical Solution of Partial Differential Equations: Finite Difference Methods*, 3rd edn, Oxford University Press.

Stone, H. A. (1990), 'A simple derivation of the time-dependent convective-diffusion equation for surfactant transport along a deforming interface', *Phys. Fluids A* **2**, 111–112.

Sullivan, B. D., Whitmer, D., Nichols, K. K., Tomlinson, A., Foulks, G. N., Geerling, G., Pepose, J. S., Kosheleff, V., Porreco, A. and Lemp, M. A. (2010), 'An objective approach to dry eye disease severity', *Invest. Ophthalmol. Vis. Sci.* **51**, 6125–6130.

Tietz, N. W. (1995), *Clinical Guide to Laboratory Tests*, 3rd edn, W. B. Saunders.

Tiffany, J. M. (1990*a*), 'Measurement of wettability of the corneal epithelium I. particle attachment method', *Acta Ophthalmol.* **68**, 175–181.

Tiffany, J. M. (1990*b*), 'Measurement of wettability of the corneal epithelium II. contact angle method', *Acta Ophthalmol.* **68**, 182–187.

Tiffany, J. M. (1991), 'The viscosity of human tears', *Int. Ophthalmol.* **15**, 371–376.

Tomlinson, A., Doane, M. G. and McFadyen, A. (2009), 'Inputs and outputs of the lacrimal system: review of production and evaporative loss', *Ocul. Surf.* **7**, 186–198.

Tomlinson, A., Khanal, S., Ramesh, K. and et al (2006), 'Tear film osmolarity as a referent for dry eye diagnosis', *Invest. Ophthalmol. Vis. Sci.* **47**, 4309–4315.

Trefethen, L. N. (2000), *Spectral Methods in MATLAB*, SIAM, Philadelphia.

Tutt, R., Bradley, A., Begley, C. and Thibos, L. (2000), 'Optical and visual impact of tear break-up in human eyes', *Invest. Ophthalmol. Vis. Sci.* **41**(13), 4117–4123.

Versura, P., Profazio, V. and Campos, E. C. (2010), 'Performance of tear osmolarity compared to previous diagnostic tests for dry eye diseases', *Curr. Eye Res.* **35**, 553–564.

Wang, J., Fonn, D., Simpson, T. L. and Jones, L. (2003), 'Precorneal and pre- and postlens tear film thickness measured indirectly with optical coherence tomography', *Invest. Ophthalmol. Vis. Sci.* **44**, 2524–2528.

Webber, W. R. S. and Jones, D. P. (1986), 'Continuous fluorophotometric method measuring tear turnover rate in humans and analysis of factors affecting accuracy', *Med. Biol. Eng. Comput.* **24**, 386–392.

Winter, K. N., Anderson, D. M. and Braun, R. J. (2010), 'A model for wetting and evaporation of a post-blink precorneal tear film', *Math. Med. Biol.* **27**, 211–225.

Wu, Z., Begley, C. G., Port, N., Bradley, A., Braun, R. J. and King-Smith, P. E. (2015), 'The effects of increasing ocular surface stimulation on blinking and tear secretion', *Invest. Ophthalmol. Vis. Sci.* **56**, 4211–4220.

Yokoi, N., Takehisa, Y. and Kinoshita, S. (1996), 'Correlation of tear lipid layer interference patterns with the diagnosis and severity of dry eye', *Am. J. Ophthalmol.* **122**, 818824.

Zhang, L., Matar, O. K. and Craster, R. V. (2003), 'Analysis of tear film rupture: Effect of non-Newtonian rheology', *J. Coll. Interface Sci.* **262**, 130–48.

Zhang, L., Matar, O. K. and Craster, R. V. (2004), 'Rupture analysis of the corneal mucus layer of the tear film', *Molec. Sim.* **30**, 167–72.

Zubkov, V. S., Breward, C. J. and Gaffney, E. A. (2012), 'Coupling fluid and solute dynamics within the ocular surface tear film: a modelling study of black line osmolarity', *Bull. Math. Biol.* **74**, 2062–2093.

Appendix

A. Governing dimensional equations

A.1 *Inside the film*

For the axisymmetric geometry the position vector components are (r', z') and the corresponding velocity components are (u', w'). (Primes denote dimensional variables or operators.) In our mathematical modeling, we consider the tear film as as incompressible Newtonian liquid with viscosity μ and density ρ, as well as diffusivities of solutes D_i, with $i = o, f$ for osmolarity and fluorescein, respectively. The film is $0 < z' < h'(r', t')$, and the flow is assumed to be axisymmetric. Conservation of mass for the incompressible fluid is

$$\nabla' \cdot \mathbf{u}' = 0 \tag{A.1}$$

Conservation of momentum in this setting is

$$\rho \left(\partial_{t'} \mathbf{u}' + \mathbf{u}' \cdot \nabla \mathbf{u}' \right) = -\nabla p + \mu \nabla'^2 \mathbf{u}' \tag{A.2}$$

In the above equations p' is the pressure, and $\phi' = A_*/(h')^3$ with $A_* < 0$ is the van der Waals contribution causing wetting and preventing complete dry-out of the film.

The conservation of solute (osmolarity) requires

$$\partial_{t'} c' + \nabla' \cdot (\mathbf{u}' c') = D_o \nabla'^2 c'; \tag{A.3}$$

c' is the solute (osmolarity). For the fluorescein concentration f', we require

$$\partial_{t'} f' + \nabla' \cdot (\mathbf{u}' f') = D_f \nabla'^2 f'. \tag{A.4}$$

A.2 *At the film/substrate (cornea) interface*

At $z' = 0$, we need to satisfy no slip

$$u' = 0, \tag{A.5}$$

and osmosis through a perfect semipermeable membrane

$$w' = P_o V_w (c' - c_0). \tag{A.6}$$

Here P_o is the permeability of the membrane, V_w is the molar volume, c_0 is the isosmolar (serum) concentration. Note that the contribution of the fluorescein concentration to osmosis is neglected; the details may be found in Braun et al. (2015).

We also have the flux boundary condition for the solute

$$D_o \partial_z' c' + w' c' = 0. \tag{A.7}$$

For f', we have

$$D_f \partial_z' f' + w' f' = 0. \tag{A.8}$$

A.3 *At the film/air interface*

At $z' = h'$, we need to satisfy the kinematic condition

$$\rho \left(h'_{t'} + u' \nabla'_{II} h' - w' \right) / (1 + |\nabla'_{II} h'|^2)^{1/2} = -J' \tag{A.9}$$

where the mass flux of evaporation is given by the constitutive relation

$$J' = \rho v_0 J'_f(r'/\ell) + \alpha_0 (p' - p'_v). \tag{A.10}$$

∇'^2_{II} is the gradient in the plane of the substrate parallel to $z = 0$. We assume that there is an isothermal film; α_0 is effectively α/K from Ajaev and Homsy. We assume that the pressure causes deviation from a uniform rate of evaporation of ρv_0 where v_0 is a measured thinning rate of the tear film. We will use the ρv_0 to nondimensionalize the evaporative mass flux where $J'_f(r'/\ell) = \rho v_0$ is the uniform evaporation rate; when it is not uniform, the scaling is with the peak evaporation rate.

The normal stress condition is given as

$$p' - p'_v = - \left(\gamma \nabla_s \cdot \mathbf{n}' + \frac{A^*}{h'^3} \right). \tag{A.11}$$

where $\nabla_s = (I - \mathbf{nn}) \cdot \nabla$ and $\mathbf{n} = (-\nabla'_{II} h', 1)/(1 + |\nabla'_{II} h'|^2)^{1/2}$ is the outward normal to the free surface (Stone, 1990). Also, γ is the surface energy of the film which will depend on the insoluble surfactant surface concentration. The no flux of solutes (osmolarity) across the film surface is given by

$$D_o \mathbf{n} \cdot \nabla' c' + \mathbf{n} \cdot \mathbf{u}' c' = 0. \tag{A.12}$$

Similarly for the fluorescein concentration,

$$D_f \mathbf{n} \cdot \nabla' f' + \mathbf{n} \cdot \mathbf{u}' f' = 0. \tag{A.13}$$

B. Lubrication equations, (axisymmetric) spot case

The thin film equations may be derived by adapting previous approaches to the axisymmetric case (Braun, 2012; Jensen and Grotberg, 1993; Zubkov et al., 2012). The governing equations are nondimensionalized using the scalings (3.1).

The resulting set of axisymmetric system of equations in the liquid region $0 < z < h(r,t)$ are as follows.

$$\frac{1}{r} \partial_r (ru) + \partial_z w = 0, \tag{B.1}$$

$$\varepsilon \mathrm{Re} \left(\partial_t u + u \partial_r u + w \partial_z u \right) = \varepsilon^2 \left[\frac{1}{r} \partial_r (r \partial_r u) - \frac{u}{r^2} \right] + \partial_z^2 u - \partial_r p, \tag{B.2}$$

$$\varepsilon^3 \mathrm{Re} \left(\partial_t w + u \partial_r w + w \partial_z w \right) = \varepsilon^4 \left[\frac{1}{r} \partial_r (r \partial_r w) \right] + \varepsilon^2 \partial_z^2 w - \partial_z p, \tag{B.3}$$

$$\partial_t c + u \partial_r c + w \partial_z c = \mathrm{Pe}_c^{-1} \left[\frac{1}{r} \partial_r (r \partial_r c) + \varepsilon^{-2} \partial_z^2 c \right], \tag{B.4}$$

$$\partial_t f + u\partial_r f + w\partial_z f = \mathrm{Pe}_f^{-1}\left[\frac{1}{r}\partial_r(r\partial_r f) + \varepsilon^{-2}\partial_z^2 f\right], \tag{B.5}$$

where $\mathrm{Re} = \rho v_0 \ell / \mu$ is the Reynolds number.

The boundary conditions on $z = 0$ are

$$u = 0, \tag{B.6}$$

$$w = P_c(c-1), \tag{B.7}$$

$$\varepsilon^{-2}\,\mathrm{Pe}_c^{-1}\partial_z c = wc. \tag{B.8}$$

The boundary conditions on $z = h(r,t)$ are

$$(\partial_t h + u\partial_r h - w)/(1 + \varepsilon^2|\nabla_{II}h|^2)^{1/2} = -J, \tag{B.9}$$

$$(\mathrm{Pe}_c\varepsilon)^{-1}\left(-\varepsilon^2\partial_r h\partial_r c + \partial_z c\right) = (u\partial_r h - w)c, \tag{B.10}$$

where

$$J = J_f(r) - \alpha\left[\frac{1}{r}(rh_r)_r + \frac{A}{h^3}\right] \tag{B.11}$$

and the forms of J_f used in this study are given by Eqns. (3.11) and (3.12).

The leading order equations for all but the solute equations are obtained by setting $\varepsilon = 0$. Integrating mass conservation from 0 to h and applying Leibnitz rule yields

$$w(r,h,t) - u(r,h,t)\partial_r h - w(r,0,t) + \frac{1}{r}\partial_r\int_0^h (ru)dz = 0 \tag{B.12}$$

The first two terms may be eliminated using the kinematic condition and the third term can be eliminated using (B.6) and (B.7) at $z = 0$, so that

$$\partial_t h + J - P_c(c-1) + \frac{1}{r}\partial_r(rh\bar{u}) = 0 \tag{B.13}$$

where

$$\bar{u} = h^{-1}\int_0^h u(r,z,t)dz. \tag{B.14}$$

The approximate velocity component u for stress free case is

$$u(z) = -\left(\frac{z^2}{2} - zh\right)\partial_r p. \tag{B.15}$$

and for the tangentially immobile case, the velocity component along the film is

$$u(z) = -\left(\frac{z^2}{2} - \frac{zh}{2}\right)\partial_r p. \tag{B.16}$$

For the solute (osmolarity) equation we proceed by expanding $c(r,z,t)$ as follows

$$c = c_0(r,t) + \varepsilon^2 c_1(r,z,t) + O(\varepsilon^4) \tag{B.17}$$

Substituting (B.17) in to (B.4) and collecting the leading order coefficients yields

$$\partial_z^2 c_0 = 0, \tag{B.18}$$

which results in $c_0 = c_0(r,t)$. Next, we collect the next order that gives us the following equation

$$\partial_z^2 c_1 = \text{Pe}_c \left(\partial_t c_0 + u \partial_r c_0 \right) - \left[r^{-1} \partial_r (r \partial_r c_0) \right] \tag{B.19}$$

Integrating equation (B.19) over $0 \leqslant z \leqslant h$ gives

$$\partial_z c_1(r,h,t) - \partial_z c_1(r,0,t) = \text{Pe}_c \left[h \partial_t c_0 + u \cdot \partial c_0 \right] - h \left[r^{-1} \partial_r (r \partial_r c_0) \right]. \tag{B.20}$$

The boundary conditions at $O(\varepsilon^2)$ are

$$\partial_z c_1(r,0,t) = \text{Pe}_c w c_0(r,0,t) \tag{B.21}$$

and

$$\partial_z c_1(r,h,t) = \text{Pe}_c c_0(r,h,t) J + \nabla h \cdot \nabla c_0(r,h,t); \tag{B.22}$$

substitution yields the PDE for c_0, the leading order osmolarity. After dropping the suscript, we have

$$h \left(\partial_t c + \bar{u} \partial_r c \right) = \text{Pe}_c^{-1} \left[r^{-1} \partial_r (r \partial_r c) \right] + Jc - P_c(c-1)c. \tag{B.23}$$

The equation for fluorescein concentration can be derived similarly, and is given by

$$h \left(\partial_t f + \bar{u} \partial_r f \right) = \text{Pe}_f^{-1} \left[r^{-1} \partial_r (r \partial_r f) \right] + Jf - P_c(c-1)f. \tag{B.24}$$

C. Cartesian Case for (Linear) Streaks

The planar or Cartesian case for streaks of TBU is considered on $0 < x < x_L$ with symmetry at $x = 0$ and homogeneous Neumann BCs at $x = x_L$. The same nondimensionalization is used as in the spot case.

The liquid region is in $0 < z < h(x,t)$ and $0 \leqslant x \leqslant x_L$. Let (u,w) be the respective velocity components in the (x,z) directions. The lubrication equations may be derived using a similar approach as for the spot, as has been described elsewhere (Braun, 2012; Braun et al., 2015). The nondimensional thin film equations for streaks are as follows:

$$\partial_t h = -\partial_x(h\bar{u}) + P_c(c-1) - J, \tag{C.1}$$

$$h(\partial_t c + \bar{u}\partial_x c) = Pe_c^{-1}\partial_x(h\partial_x c) - P_c(c-1)c + Jc, \tag{C.2}$$

$$h(\partial_t f + \bar{u}\partial_x f) = Pe_f^{-1}\partial_x(h\partial_x f) - P_c(c-1)f + Jf, \tag{C.3}$$

where

$$u = \left(z^2 - zh \right) \partial_x p / 2, \quad p = -\partial_x^2 h - Ah^{-3} \tag{C.4}$$

and

$$\bar{u} = h^{-1} \int_0^h u(x,z,t)dz = -\frac{h^2}{12}\partial_x p. \tag{C.5}$$

C.1   *Evaporation functions*

The dimensional equations for evaporation are

$$J' = \rho v_0 f(x'/\ell) + \alpha_0 \left[p' - p_v'\right] \quad \text{and} \quad p' - p_v' = -\left[\gamma \partial_x^2 h + A^* h^{-3}\right]. \tag{C.6}$$

Nondimensionally,

$$J = J_f(x) - \alpha \left[\partial_x^2 h + A h^{-3}\right]. \tag{C.7}$$

The fixed evaporation distribution is the same as for the radial case except that r and r_w are replaced with x and x_w, respectively. For the Gaussian case,

$$J_f(x) = v_b + (1 - v_b)e^{-(x/x_w)^2/2} \tag{C.8}$$

The standard deviation x_w will be used to indicate the width of the evaporation distribution and the resulting streak. The background thinning rate $v_b = v_1/v_0$ is the relative to the peak rate; the dimensional value is assumed to be 1μm/min in all cases. For the tanh case,

$$J_f(x) = v_b + (1 - v_b)\left[1 - \tanh\left(\frac{x - x_w}{2x_0}\right)\right] \tag{C.9}$$

We use $x_0 = 0.05$ to keep the transition narrow relative to the domain size. The mass lost can be kept the same if x_w for the tanh case is $\sqrt{2}$ larger than the Gaussian case.

C.2   *Lubrication equation BCs and ICs*

The boundary conditions are symmetry at $x = 0$, which result in the following homogeneous Neumann conditions:

$$\partial_x h(0,t) = \partial_x p(0,t) = \partial_x c(0,t) = \partial_x f(0,t) = 0. \tag{C.10}$$

The no flux conditions at $x = x_L$ result in

$$\partial_x h(x_L,t) = \partial_x p(x_L,t) = \partial_x c(x_L,t) = \partial_x f(x_L,t) = 0. \tag{C.11}$$

The initial values are uniform in space, with

$$h(x,0) = c(x,0) = 1, \ f(x,0) = f_0, \tag{C.12}$$

and the consistent value for the pressure is found from its definition and used for the initial condition.